Chapter 2
Introduction and Fundamental Theory

In this chapter the fundamentals involved in coherent imaging with laser generated XUV light are presented. The first Sect. 2.1 introduces high harmonic generation, which is the process that is used throughout this thesis to generate coherent XUV light. In Sect. 2.2 some imaging theory and a mathematical description for the diffraction of light by matter will be introduced. A major issue in CDI is the so-called *phase problem*, which arises from the fact that one can only measure intensities with a physical detector in an experiment. For the reconstruction of an object, however, the phase of the light field must be known. If sufficient care to some geometric constraints, as presented in Sect. 2.2.4, is taken, one can retrieve the phase of the light field by means of iterative algorithms, which are introduced in Sect. 2.3. Another approach for coherent imaging is digital in-line holography, which is a technique where the phase of the light field is already encoded in the fringes measured in the far-field with a detector. The fundamentals about digital in-line holography are presented in Sect. 2.4. A chapter summary and view at other modern imaging techniques, which are not used in this thesis, will conclude this chapter

2.1 High Harmonic Generation in Gases

In this section the basic nonlinear process to generate short wavelength light will be introduced. Therefore, first an electro-magnetic wave impinging on a material is considered as the interaction between light and matter is discussed. The feedback from the material to the electric field ($\mathbf{E}(\mathbf{r}, t)$)[1] is expressed by a linear dependence of the polarisation $\mathbf{P}$ on the electric field connected by the susceptibility χ. This linear behavior corresponds to bound electrons moving in the Coulomb potential of the atoms, and experiencing a small perturbation of their motion by the laser field. This small perturbation can be treated as a small amplitude electron bouncing in a

[1] Throughout this thesis vectors and vectorial quantities will be denoted by a boldface typeset, e.g. $\mathbf{r}$. The modulus of $\mathbf{r}$ is denoted simply as r.

M.W. Zürch, *High-Resolution Extreme Ultraviolet Microscopy*,
Springer Theses, DOI 10.1007/978-3-319-12388-2_2

harmonic potential approximating the atomic or molecular potential in the vicinity of the stationary orbit. However, this approximation is not valid for higher intensities and thus the relation between the polarization and the electric field turns from linear to a power series in χ [1]

$$\mathbf{P}(\mathbf{r},t)_{\mathrm{NL}} \propto \chi^{(1)}(\omega)\mathbf{E}(\mathbf{r},t) + \chi^{(2)}(\omega)\mathbf{E}^2(\mathbf{r},t) + \chi^{(3)}(\omega)\mathbf{E}^3(\mathbf{r},t) + \cdots, \quad (2.1)$$

where $\chi^{(n)}$ represents the n-th order susceptibilities. For non-centrosymmetric media, all even terms in this series are equal to zero. The nonlinear response of the polarization results in a zoo of effects that kick in once a certain intensity, depending on material parameters, is reached. The coefficients $\chi^{(n)}$ can be linked to a specific nonlinear effect, e.g. harmonic generation. More details are discussed in [2].

The most used nonlinear effect is frequency conversion, which can be anything from multiple harmonic generation to complicated frequency mixing [1]. However, due to absorption and usually decreasing $\chi^{(n)}$ for increasing n for typical materials, the generation of harmonics much beyond the third order is not efficient.

Expression 2.1 is the basis for conventional perturbative nonlinear optics. It is obvious that the nonlinear motion of bound electrons is not able to provide harmonics with the energy of quanta larger than the ionization potential of the atom or molecule. To overcome this limitation and to enable frequency conversion to the XUV and X-ray spectral range, a new mechanism inevitably involving the ionization of the medium in a high intensity laser field should be proposed. Such a mechanism was proposed in [3, 4] and is called *high-order harmonic generation* (HHG) in gases. This highly nonlinear process allows to generate coherent light with photon energies up to the kiloelectronvolt level [5, 6]. The principal structure of an HHG spectrum is depicted in Fig. 2.1. The intensities of the lower order odd harmonics only, with any energy of quantas up to the ionization potential of the atom, follow the perturbative regime predicted by Eq. 2.1. These lower order harmonics are followed by the so called plateau, where the yield of the harmonics is about constant over a large wavelength span. A cut-off at the high energetic end of the spectrum relates to the shortest produced wavelengths.

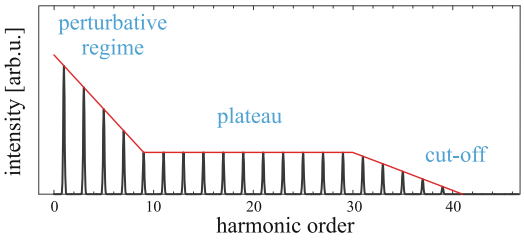

Fig. 2.1 Schematic HHG spectrum. The intensity of the lower order harmonics follows a perturbative regime, which is followed by a plateau featuring about equally intense harmonics. The cut-off marks the highest photon energies generated

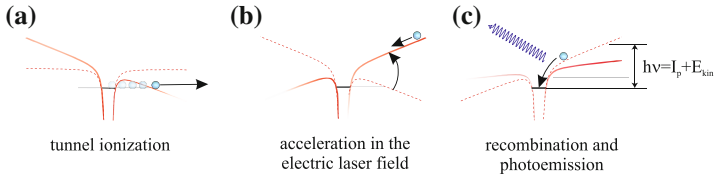

Fig. 2.2 The three-step-model in brief: **a** An electron tunnels out of the parent ion due to the Coulomb potential (*dotted red line*) of the atom being deformed (*solid red line*) by the electric field of the laser. **b** The electron accelerates in the laser field and gains kinetic energy. **c** The electron recombines with the parent ion and a photon with a energy $h\nu$ equivalent to the electrons kinetic energy E_{kin} and the ionization potential I_p of the ion is emitted

In the early 1990s Krause et al. [7] and Corkum [8] developed a simple model that is able to describe the plateau and cut-off structure for a single-atom using a semi-classical approach. The so-called three-step-model consists of three parts: ionization, acceleration, and recombination of an electron, as depicted in Fig. 2.2.

2.1.1 Ionization

In order to estimate the electric field that is needed to significantly modify the Coulomb potential of an atom, one can calculate the electric field of a bound electron in a hydrogen atom. This is done by using Bohr's atomic model and the Bohr radius a_0 to calculate the electric field as

$$E_a = \frac{e}{4\pi\epsilon_0 a_0^2} = 5 \times 10^{11}\,\text{V/m}. \tag{2.2}$$

From this one gets an estimate of the intensity of a laser field having an equivalent electric field

$$I_a = \frac{1}{2}\epsilon_0 c E_a^2 = 3.51 \times 10^{16}\,\text{W/cm}^2. \tag{2.3}$$

Such intensities are easily reachable with modern ultrafast lasers. Using the single active electron (SAE) approximation [9], one can write the combined potential experienced by the single electron and the laser field as

$$V(\mathbf{r}, t) = -\frac{e^2}{4\pi\epsilon_0|\mathbf{r}|} + e\mathbf{E}(t)\mathbf{r}. \tag{2.4}$$

Obviously, a significant modification of the electron motion in the atom can only take place if the intensity of the laser field is high enough, i.e. on the order given in Eq. 2.3.

According to Eq. 2.4, the combined potential features a time-dependent barrier. The width of this barrier r_B can be estimated as $er_B E \sim I_p$, where I_p is the ionization potential of the atom. Using the characteristic velocity of the electron motion in the atom $v_a \sim \sqrt{\frac{2I_p}{m_e}}$, one can introduce a characteristic tunneling time $\tau \sim \frac{r_B}{v_a} \sim \sqrt{\frac{2m_e I_p}{e^2 E^2}}$. The regime of ionization is determined by the ratio of the tunneling time to the optical cycle. A corresponding parameter, known as the *Keldysh parameter*, to distinguish these regimes was introduced by Keldysh [10] and is defined as

$$\gamma = \tau\omega = \sqrt{\frac{I_p}{2U_p}}, \tag{2.5}$$

where ω is the laser frequency and $U_p = \frac{e^2 E_0^2}{4m_e\omega^2}$ is the ponderomotive potential, which is the mean kinetic energy of a free electron oscillating in the monochromatic laser field with an amplitude E_0. When $\gamma \gg 1$, which corresponds to relatively low laser intensities or short laser wavelengths, the electron does not have sufficient time to tunnel through the potential barrier within an optical cycle. Instead, ionization proceeds via absorption of multiple optical photons. This is the so-called *multiphoton ionization* regime. It is typical for high intensity laser pulses in the visible or UV spectral range. In the opposite case $\gamma \ll 1$, ionization occurs on the sub-cycle time scale due to electron tunneling through the potential barrier. For the near-infrared laser wavelength 800 nm, as used in the experiments in this thesis, ionization occurs in a mixed regime, since $\gamma \sim 1$.

2.1.2 Acceleration

The generation of a free electron is followed by acceleration (Fig. 2.2b) in the laser field $E = E_0 \cos(\omega t + \phi)$. Since ionization occurs in the electric field of the laser pulse, which is comparable to the characteristic atomic field (Eq. 2.2), the Coulomb attraction force from the ion on the free electron is much weaker than the electric force of the laser pulse. That is why the influence of the ion on the electron motion can be neglected and analysis can be done for trajectories of a free electron in the monochromatic electric field. Hence, one can calculate the movement of the electron that is born at a phase ϕ of the laser field, assuming the electron being at rest $v_0 = 0$ after tunneling, by

$$v(t) = \int_0^t -\frac{e}{m_e} E(t)\mathrm{d}t = -\frac{E_0 e}{m\omega}\{\sin(\omega t + \phi) - \sin\phi\}, \tag{2.6}$$

$$x(t) = \int_0^t v(t)\mathrm{d}t = \frac{E_0 e}{m_e\omega^2}\{\cos(\omega t + \phi) - \cos(\phi) + \sin(\phi)t\}. \tag{2.7}$$

The kinetic energy of the electron can be calculated from Eq. 2.6, which, after averaging over an optical cycle, results in the ponderomotive potential introduced before. As a consequence $U_p \propto I$. The electrons can either drift away or recollide with the parent ion, which can be found by calculating the trajectory of the electrons for different phases ϕ in Eq. 2.7. This is discussed in full for instance in [11].

2.1.3 Recombination

When an electron recollides with its parent ion, three different processes might occur with different probability: (i) elastic rescattering of the electron on the ion; (ii) inelastic scattering with excitation or ionization of bound electrons in the ion; (iii) recombination of the electron with the parent ion. If recombination occurs a photon is emitted (Fig. 2.2c), having the combined kinetic energy of the electron and the ionization potential of the ion

$$\hbar\omega = I_p + E_{\text{kin}}. \tag{2.8}$$

According to Eq. 2.6 the kinetic energy of the electron depends on the time it spends in the laser field. This obviously depends on the phase ϕ of the laser field at the time when the atom was ionized. Solving the equation of motion of the electron (Eq. 2.6) with $x(t) = 0$ for different phases ϕ one gets a maximum kinetic energy for $\phi \approx 18°$. Thus $E_{\text{kin}} = 3.17 \cdot U_p$ is the upper limit for the energy of the emitted photon by the electron. Together with the ionization potential of the atom one gets the so-called cut-off energy

$$\hbar\omega_{\text{cutoff}} = I_p + 3.17U_p. \tag{2.9}$$

Despite the simplicity of the three-step-model and its deterministic connection of classic and quantum mechanical effects, it is able to describe the features observed in HHG. The structure of the cut-off, the plateau behavior (Fig. 2.1), and the existence of only odd harmonics, due to every half-cycle causing recollisions, are well explained. A more rigorous quantum mechanical model for HHG was developed by Lewenstein et al. [12], which will not be discussed in depth in this thesis.

Other general properties one has to mention when dealing with HHG is that the light produced is highly coherent and emitted in a beam having typically a smaller divergence compared to the driving laser beam [13, 14]. The photon flux generated with HHG is low compared to synchrotrons or free-electron lasers. Limiting for the photon flux is the low conversion efficiency. The highest reported HHG conversion efficiencies are in range of $\approx 10^{-5}$ [15–17]. As with other nonlinear optical processes phase matching, i.e. matching the phase velocity of the fundamental light with the phase velocity of the generated harmonics, is one of the main limiting issues. Another important issue for microscopy with high harmonics beside the flux is the bandwidth of each harmonic. The bandwidth is getting narrower the more optical cycles contribute to the signal. Thus long driving pulses generate narrowband harmonics as

they are essential for high resolution imaging as will be shown in Sect. 2.2.4. The pulse duration of the harmonics emitted is intrinsically shorter than the driving laser pulse and can reach the attosecond level [18].

2.2 Coherent Diffraction Imaging Theory

After the introduction of HHG for frequency up-conversion, the topic of this section will lead towards the application of those unique light pulses for microscopy. First, the basic principles of diffraction of light by matter will be discussed. Then specific problems and methods used in CDI to solve the so-called *phase problem* will be introduced. At the end of this section a closer look at geometric considerations one has to bear with when targeting the implementation of a CDI experiment in the lab will be taken. It is worth mentioning that direct imaging with Fresnel zone plates [19] has been done for decades at synchrotrons [20] and more recently using HHG sources [21], however, the resolution is limited due to the limited resolution in electron beam lithography for producing the zone plates. Further, the bandwidth of typical HHG pulses is limiting the usability of Fresnel zone plates.

2.2.1 Coherence Properties of a Light Field

An important measure for imaging purposes is the coherence. Coherence is a property of the light field giving information about how well defined the phase relation between different parts of the electromagnetic radiation is either in space or time. These are referred to as the spatial and temporal coherence, respectively. Spatial coherence describes the phase relation between two separated points in a plane perpendicular to the propagation direction [22]. Temporal coherence on the other hand describes a defined phase relation between two points separated in time, i.e. parallel to the propagation direction. At this stage one can already conclude that plane waves have perfect spatial coherence, since they have the same phase at all points in planes perpendicular to the propagation direction. In reality however, one always has a source of light that has a finite size, i.e. it emits spherical waves which can be approximated as plane waves only for large distances from the source. Thus, as shown in the seminal book from Attwood [22], one can relate the spatial coherence of a light source to its spatial size and its emission characteristics, i.e. the divergence $\triangle\theta$ of the radiation emitted. A measure for this is the transverse coherence length ξ_t

$$\xi_t = z\triangle\theta = \frac{z\lambda}{2\pi d}, \tag{2.10}$$

where z is the distance from the source to the plane of observation, λ is the wavelength and d is the source size. A way to measure spatial coherence is to measure with a

Young's double slit with a variable distance between the slits. The wider the slits are separated, the wider is the separation of the sampling points on the wave that impinges on the double slit. If the separation between the slits becomes greater than ξ_t one observes decreasing contrast on the fringes in the interference pattern in the far-field behind the double slit. In a similar manner, for coherent imaging one finds that spatial coherence is limiting the size of typical samples that can be imaged. This is because if samples are significantly larger than ξ_t one cannot expect clearly resolved fringes in the far-field and, thus, cannot resolve the phase as will be presented in Sect. 2.2.3. What makes the estimation of the spatial coherence according to Eq. 2.10 difficult in the practical application of CDI is the fact that typically the light from a source is refocused and the sample is placed in the focus. Hence z would be zero and one cannot use Eq. 2.10, which only applies for a divergent light field. Thus a more useful interpretation, but less measurable, is that the spatial coherence is related to the beam quality, i.e. one should optimize for a Gaussian-shaped focal spot with an ideally flat phase front.

Temporal coherence on the other hand is related to the bandwidth of the light field. This can be intuitively understood again by analyzing a Young's double slit. Since different wavelengths are diffracted under different angles one gets more smearing (broadening) of the fringes and therefore less contrast the larger the bandwidth of the incoming light field becomes. The effect increases for larger diffraction angles, i.e. larger distance from the center of the pattern. The temporal coherence can be quantified by the longitudinal coherence length ξ_l

$$\xi_l = \frac{\lambda^2}{2\triangle\lambda}. \tag{2.11}$$

$\triangle\lambda$ denotes the full width half maximum (FWHM) bandwidth of the source.

Often temporal coherence measurements are discussed with Michelson interferometers in the way that changing the path length of one interferometer arm more than ξ_l the interference is lost due to the missing phase relation between the interfering light fields. Here temporal coherence is discussed at the far-field interference pattern of a double slit. Comparing this to the discussion on spatial coherence one finds that temporal coherence effects the far-field pattern of the object, i.e. the double slit, in a similar way as spatial coherence. The only difference is that temporal coherence is more limiting at higher diffraction angles, i.e. the achievable resolution, while spatial coherence is limiting the field of view. Thus in a CDI experiment both coherence measures are of special importance.

2.2.2 Diffraction of Light Waves at Matter

In this section the basic concepts of diffraction of light waves at matter will be discussed. This field is very complex and cannot be covered in depth within this thesis. Hence, in this work the focus will be on a few principles and a few important

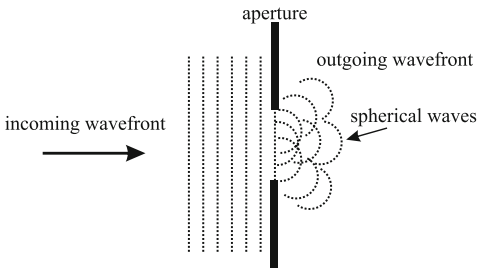

Fig. 2.3 The Huygens-Fresnel principle describes the diffraction of light as the superposition of spherical waves that emerge from an object. In the presented case this is a simple aperture

formulas to illustrate the main effects that are relevant for CDI. A more detailed discussion and further reading can be found for instance in the textbook of Jackson et al. [23]. Here the notation given in [24] will be followed, hence electric fields will be denoted by U.

An intuitive picture of diffraction is given by the Huygens-Fresnel principle (Fig. 2.3). It states that every part of a wavefront emerging from an obstacle can be considered as the center of a spherical wave. Thus the field at later points, after a certain propagation, can be described by the superposition of all spherical waves that propagated the given distance. The superposition of coherent wavefronts usually gives rise to interference effects and hence produces a certain intensity distribution that is usually called a *diffraction pattern*. So the Huygens-Fresnel principle describes the principal effects, however, the drawback is obvious, since one would need an infinite number of waves to be propagated and interfered to determine a diffraction pattern of an actual object. Another consequence of the Huygens-Fresnel principle is that a diffraction pattern that one can expect behind an aperture depends on the distance between the aperture and the plane of observation. For distances close to the aperture ($z \sim a$, where a is the aperture size), geometrical optics can be applied to describe the field structure. Going further away the diffraction pattern evolves quickly as a function of the distance since the interference of the spherical waves starts to build up. This is called Fresnel diffraction. For distances far from the object the spherical waves can be estimated as plane waves having different phases, thus the diffraction pattern does not change but merely increases in size. This case is called Fraunhofer diffraction. The transition from Fresnel to Fraunhofer diffraction is not abrupt. One can estimate the distance z for which the Fresnel regime changes into the Fraunhofer regime as

$$z \approx \frac{a^2}{\lambda}, \tag{2.12}$$

where a is the aperture size and λ is the wavelength.

This is a rather qualitative view on diffraction. In next part of this section a quantitative description of the diffraction of an arbitrary object will be derived. As shown in [24] one can derive

$$U(P) = \frac{1}{4\pi} \iint_S \left[U \frac{\partial}{\partial \mathbf{n}} \left(\frac{\exp(-i\mathbf{kr})}{r} \right) - \frac{\exp(-i\mathbf{kr})}{r} \frac{\partial U}{\partial \mathbf{n}} \right] dS \tag{2.13}$$

from the Huygens-Fresnel principle, where U is a solution of the Helmholtz equation at a point of observation P, with $\mathbf{n}$ being a unit vector normal to the emitting surface S, $\mathbf{r}$ being the vector from S to P and $\mathbf{k}$ being the wavevector. Equation 2.13 is called the Kirchhoff diffraction integral. If one now assumes to have an aperture on an otherwise opaque screen that is illuminated from one side and the observation plane is in the halfspace on the other side, one can derive [24] the Fresnel-Kirchhoff diffraction formula

$$U_K(P) = \frac{iU_0}{\lambda} \iint_{\Sigma} \frac{\exp[-i\mathbf{k}(\mathbf{r}+\mathbf{s})]}{\mathbf{rs}} \frac{[\cos(\mathbf{n},\mathbf{s}) - \cos(\mathbf{n},\mathbf{r})]}{2} dS. \tag{2.14}$$

In Eq. 2.14 $\mathbf{s}$ denotes the vector from the aperture $\sum$ to the source and $\mathbf{r}$ denotes the vector from the aperture to the point of observation P. The integration is done over $\sum$ within the halfspace S enclosing P. The Fresnel-Kirchhoff diffraction formula is still somewhat too general [24] and contains some mathematical irregularities. RAYLEIGH and SOMMERFELD used certain symmetries and assumptions to simplify Eq. 2.14 further. Using their simplifications and introducing a Cartesian coordinate system (Fig. 2.4) one can now calculate the light field U_2 at a point P_2 in the observation plane

$$U_2(x_2, y_2) = \frac{i}{\lambda} \int_{-\infty}^{\infty} \iint U_1(x_1, y_1) \frac{\exp(-i\mathbf{kr})}{r} \cos(\mathbf{n}, \mathbf{r}) dx_1 dy_1, \tag{2.15}$$

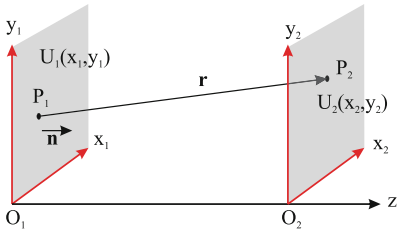

Fig. 2.4 Definition of the coordinate system. U_1 is the light field at point P_1 in the diffraction plane (x_1, y_1) and U_2 is the light field in the observation plane (x_2, y_2) at point P_2

where U_1 is the light field in the diffraction plane and $\cos(\mathbf{n}, \mathbf{r})$ is the cosine of the angle between the normal to the diffraction plane $\mathbf{n}$ and the direction of observation $\mathbf{r}$.

The factor $\frac{\exp(-i\mathbf{kr})}{r}$ describes a spherical wave originating at point P_1 and demonstrates the Huygens-Fresnel principle. Provided one knows the light field within an aperture U_1 one can calculate the diffraction pattern anywhere behind the aperture if $r \gg \lambda$ which is one of the main assumptions when deriving Eq. 2.15. For typical CDI experiments one expects a plane wave impinging on the target, thus U_1 is well defined. But also in the case of Fresnel CDI [25] one can still use Eq. 2.15 by assuming a spherical wavefront illuminating an aperture. Using the coordinate system (Fig. 2.4) the distance r between P_1 and P_2 can be expressed in Cartesian coordinates

$$r^2 = z^2 + (x_2 - x_1)^2 + (y_2 - y_1)^2 = z^2 \left[1 + \frac{(x_2 - x_1)^2 + (y_2 - y_1)^2}{z^2}\right]. \quad (2.16)$$

If the observer resides near the optical axis, which is the typical situation in CDI, one can use $(x_2 - x_1)^2 + (y_2 - y_1)^2 \ll z^2$ to simplify Eq. 2.16 to

$$r \approx z \left[1 + \frac{(x_2 - x_1)^2 + (y_2 - y_1)^2}{2z^2}\right]. \quad (2.17)$$

This paraxial approximation is called the Fresnel approximation. In this case the cosine in Eq. 2.15 becomes unity and using Eq. 2.17 one can reduce Eq. 2.15 to

$$U_2(x_2, y_2) = \frac{i \exp(-ikz)}{\lambda z} \iint_{-\infty}^{\infty} U_1(x_1, y_1) \exp\left[-ik \frac{(x_2 - x_1)^2 + (y_2 - y_1)^2}{2z}\right] dx_1 dy_1. \quad (2.18)$$

This formula yields the diffraction pattern in the paraxial approximation, which is also called the Fresnel diffraction pattern or the near-field. Inspecting Eq. 2.18 reveals that the phase in the observation plane has a quadratic dependence on the position. This is the reason as to why the Fresnel diffraction regime is complicated and difficult to handle in imaging systems. This is particularly true if one deals numerically with such geometries.

As mentioned earlier, a more orderly diffraction pattern is expected when the observation plane is further away from the diffraction plane. In this case the quadratic terms of the coordinates in the diffraction plane in Eq. 2.17 can be neglected since $z^2 \gg x_1^2, y_1^2$. One only keeps the mixing terms and gets

$$r \approx z \left[1 + \frac{x_2^2 + y_2^2}{2z^2} - \frac{x_1 x_2 + y_1 y_2}{z^2}\right]. \quad (2.19)$$

Using this so-called Fraunhofer approximation and plugging it into the Rayleigh-Sommerfeld diffraction formula (Eq. 2.15) one gets

$$U_2(x_2, y_2) = \frac{\mathrm{i}\exp(-\mathrm{i}kz)}{\lambda z}\exp\left(-\mathrm{i}k\frac{x_2^2 + y_2^2}{2z}\right) \iint_{-\infty}^{\infty} U_1(x_1, y_1)\exp\left[\frac{\mathrm{i}k}{z}(x_1x_2 + y_1y_2)\right]\mathrm{d}x_1\mathrm{d}y_1. \tag{2.20}$$

Inspecting this Fraunhofer diffraction formula one finds that a nonlinear phase variation in the observation plane is not arising. Instead one gets a steady pattern that just expands in size over the propagation distance z. The integral essentially denotes the Fourier transform of the source field U_1.[2] This is a very important result for CDI, since using numerical implementations of the Fourier transform, e.g. Fast Fourier Transforms (FFT), one can numerically switch between the diffraction pattern in the far-field and the source field at an aperture. This is the basis for iteratively solving the phase problem as will be explained in the subsequent section.

In summary the discussion started with the general Huygens-Fresnel principle that essentially describes diffraction as the sum of point sources originating at the surface of the diffracting object. Putting this into a mathematical description by integrating over all spherical waves that leave the object, a solution that obeys the Helmholtz equation for wave propagation was found. By restricting to one halfspace and using paraxial and a few further assumptions the Fresnel diffraction formula was derived. The Fresnel diffraction formula (Eq. 2.18) is valid at any distance significantly larger than the wavelength behind an illuminated aperture a. However, for even larger distances $z \gg \frac{a^2}{\lambda}$ the Fraunhofer diffraction formula (Eq. 2.20) was found. It relates the far-field and the source field by the Fourier transform. Thus the coordinates in the far-field can be related to spatial frequencies q by

$$q_x = x/(z\lambda) \quad \text{and} \quad q_y = y/(z\lambda). \tag{2.21}$$

In terms of interpreting diffraction as an elastic scattering of photons one can interpret these spatial frequencies as the components of the momentum transfer vector $\mathbf{q}(q_x, q_y, q_z)$. The photons exiting the diffraction plane $\mathbf{k}_{\mathrm{out}}$, which will later be denoted as the object plane, experience a higher momentum change the more the propagation directions differ from the incidence direction of the photons defined by the wavevector $\mathbf{k}_{\mathrm{in}}$ of the incoming wave. Hence

$$\mathbf{q} = \mathbf{k}_{\mathrm{out}} - \mathbf{k}_{\mathrm{in}} \tag{2.22}$$

[2] In literature this field is also often referred to as the *exit surface wave*.

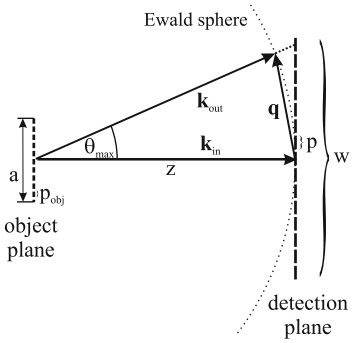

Fig. 2.5 Scattering of an incident coherent beam $\mathbf{k}_{in}$ on a planar object in the object plane (diffraction plane). The wavevector of the exiting photons $\mathbf{k}_{out}$ ends on the Ewald sphere. Since one measures a diffraction pattern in the detection plane, one can interpret the spatial frequencies as the projection of the momentum transfer vector $\mathbf{q}$ on the corresponding axis. The object plane is characterized by its spatial extent a and a sampling size, i.e. the object pixel size, p_{obj}. The detection plane is likewise characterized by the detector size w and the pixel size p. Please note that one can already see in this sketch that the Ewald sphere is projected onto the planar detector. For high scattering angles, e. g. denoted by θ_{max}, as they occur for high numerical aperture measurements, a correction of this effect is necessary. Details can be found in Sect. 3.4

gives the resulting momentum transfer vector.[3] Energy conservation imposes $|\mathbf{k}_{out}| = |\mathbf{k}_{in}|$. Hence, all scattering vectors, and thus the diffraction pattern, lie on a sphere, which in crystallography is called the Ewald sphere [27]. The Ewald sphere has thus the radius $1/\lambda$, since $k \propto 1/\lambda$. The scattering geometry is depicted in Fig. 2.5. Throughout this thesis it will be assumed that the Ewald sphere has a radius $1/\lambda$.[4] The momentum transfer $q = |\mathbf{q}|$ for a given scattering angle θ thus becomes [28][5]

$$q = \frac{2}{\lambda} \sin\left(\frac{\theta}{2}\right). \tag{2.23}$$

2.2.3 The Phase Problem

In the preceding section it was found that the object plane, i.e. the source field, and the detection plane are Fourier conjugates in the Fraunhofer approximation, which

[3] One can compare Eq. 2.22 with the well-known momentum transfer equation from elastic scattering $\triangle\mathbf{p} = \mathbf{p} - \mathbf{p}_0$ by multiplying both sides in Eq. 2.22 with $\hbar = h/2\pi$ where h is Planck's constant. If one now uses the de Broglie relation $\mathbf{p}_0 = \hbar\mathbf{k}_{in}$ and $\mathbf{p} = \hbar\mathbf{k}_{out}$ for the incident and scattered particle, respectively, it becomes clear that $\hbar\mathbf{q} = \hbar\mathbf{k}_{out} - \hbar\mathbf{k}_{in}$ is the momentum transfer vector [26].

[4] For the sake of being consistent with *most* of the literature on CDI. Hence, $|\mathbf{k}| = 1/\lambda$ is used.

[5] This equation comes from an isosceles triangle, where $c = 2a \sin(\gamma/2)$. Comparing it to the well-known Bragg's law one finds that Eq. 2.23 is equivalent to a volume grating being tilted about half the diffraction angle θ.

is almost always fulfilled for soft X-ray imaging due to the short wavelength. Thus one could retrieve the object except for a constant phase factor by a simple Fourier transform if one could sample the amplitude and the phase in the far-field. However, in all experiments that will be presented throughout this thesis an XUV sensitive charge coupled device detector (CCD, details in Chap. 3) is used to measure the diffraction patterns. Unfortunately, there are no detectors that can measure phase and amplitude spatially resolved simultaneously; instead a CCD measures only intensities, i.e. $I \propto UU^* = |U|^2$. Hence the phase information is typically lost in CDI experiments, a predicament commonly called the *phase problem*.

In 1952 Sayre published a seminal article [29] where he states that in principle the phase information can be recovered from the diffraction intensities if they are sampled densely enough. The idea behind this is the Shannon theorem [30], which essentially states that one can retrieve the phase of a signal if it is sampled at twice its frequency, the so-called *Nyquist frequency*. As shown before, one can think of the plane of a diffraction pattern as a plane of spatial frequencies. Thus the implication from Sayre's work that he continued years later [31] is that one can retrieve the phase if the continuous X-ray diffraction pattern caused by an non-periodic object is sampled sufficiently dense. This is called the oversampling of the diffraction pattern. Bates discussed in [32] that the solution of this inversion problem would be almost always unique. If one considers a sample with a diameter a one can determine the spatial Nyquist frequency to $f_{\text{Nyquist}} = a/(z\lambda)$. This would be the spatial frequency with which one would have to sample the diffraction pattern with, in order to achieve a direct conjugate relation between object plane and the diffraction pattern. If the phase problem is considered as a set of equations one would have N equations in both planes, i.e. N pixels considering a CCD. However, since every detection spot is characterized by an amplitude and a phase one has $2N$ unknowns and due to the phase problem only N, i.e. the amplitudes $\sqrt{I}$, knowns. To solve this system of equations one can, however, sample the diffraction pattern with $2\,f_{\text{Nyquist}}$, i.e. having two pixels per spatial Nyquist frequency in terms of a CCD, and have $2N$ knowns ($2N$ amplitudes). If one now uses that there are $2N$ unknowns (N amplitudes and N phases) in the object plane, one can in principle retrieve the phase [33]. In terms of an FFT this means that the object plane has a certain zero padding around the object, where amplitude and phase are known to be zero. This is depicted as two-dimensional case in Fig. 2.6.

To quantify the oversampling of a diffraction pattern one can introduce an oversampling ratio σ, which one can define in the object plane as

$$\sigma = \frac{\text{region with electron density} + \text{region without electron density}}{\text{region with electron density}}. \tag{2.24}$$

The formulation *electron density* comes from X-ray diffraction on atoms, where the dipoles of the electrons in an atom are the sources of the spherical wavelets [23]. To be consistent with most CDI literature the electron density ρ will further be used as a substitute for the source terms U in the previous section. So even for an aperture,

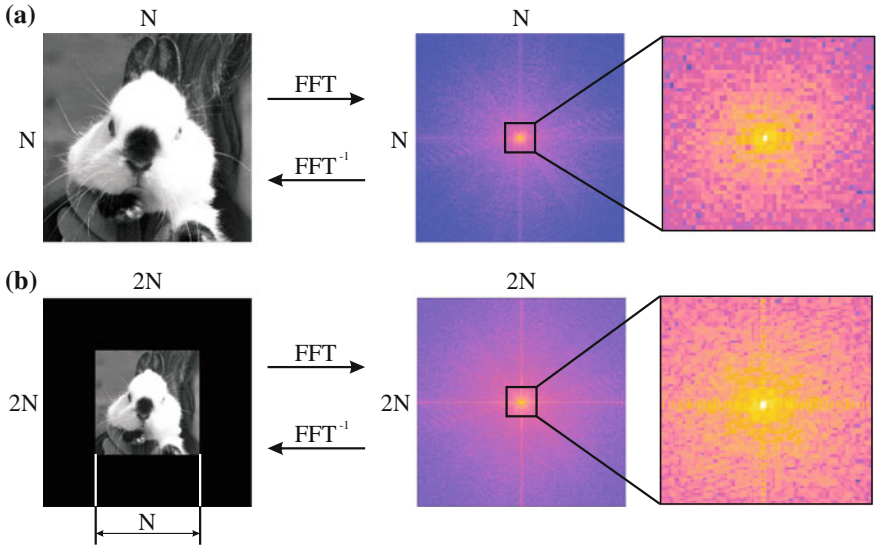

Fig. 2.6 Oversampling as condition for solving the phase problem. **a** An object that fills N by N pixels in the object plane results in a N by N pixels diffraction pattern in the Fourier transform plane. **b** If one, however, adds a zero-density region around the object, i.e. zero-padding, to $2N$ by $2N$ pixels one gets the corresponding $2N$ by $2N$ diffraction pattern. This represents a twofold oversampled diffraction pattern with $2N$ by $2N$ known amplitudes, which allow to solve the phase problem (the amplitude in the Fourier transform plane is plotted on the *right panels* on a logarithmic scale). This is because there are only N by N complex-valued unknowns in the object plane and all other pixels in the zero-density region can be set to zero. For convenience the arrays are shown at the same size, in reality the arrays in (**b**) are four times larger

where the field in the object plane can be reconstructed, one can recover the object itself through Babinet's princple [24].

According to Sayre $\sigma \geq 2$ is necessary to solve the phase problem. In the detection plane this corresponds to the number of pixels used to sample a speckle in the diffraction pattern. In two dimensions $O = \sqrt{\sigma}$ the linear oversampling degree in the detection plane can be introduced [34]

$$O = \frac{\lambda z}{ap}, \tag{2.25}$$

with λ being the wavelength, p the width of a detector pixel, z the distance between object and detection plane and a the largest spatial extent of the object. According to Eq. 2.21 this corresponds to the highest spatial frequency observed from an object related to the size of a detector pixel.

In this section it was shown that the phase problem can in principle be solved, if sufficient oversampling in the diffraction pattern is maintained. The ambiguity that is left and cannot be recovered is a lateral translation of the object, a complex conjugation,

a spatial inversion and an absolute phase shift [32]. One should note that all these considerations are only valid for the Fraunhofer regime, because the nonlinear phase evolution in the Fresnel regime, as pointed out in Sect. 2.2, would not satisfy a linear sampling theorem [34]. To maintain sufficient oversampling in an experiment, careful considerations regarding the experimental geometry are necessary. This will be covered in the following section.

2.2.4 Geometric Considerations

In the preceding section it was found that oversampling (Eq. 2.25) is a crucial requirement for CDI experiments in order to retrieve the object plane from a far-field diffraction pattern. The far-field condition was given in Eq. 2.12. In Sect. 2.2.1 the coherence properties of a light source were investigated. Hence it is beneficial to bring the findings together and have a look at the restrictions to the experimental geometry and the properties of the light source that arise from these findings. Spence et al. present a comprehensive discussion [35] on the coherence requirements of a source for proper CDI. For the transverse coherence length they found that

$$\xi_t > 2a, \tag{2.26}$$

where ξ_t is the transverse coherence length as discussed in Sect. 2.2.1 and a is the spatial extent of the object. The reason for this is that the autocorrelation function Γ of an object o

$$\Gamma(\mathbf{r}) = o(\mathbf{r}) \otimes o^*(-\mathbf{r}), \tag{2.27}$$

where $\otimes$ denotes the convolution operator, has twice the size of its spatial extent a [28]. That means that according to [35] the transverse coherence must at least be maintained over the size of the autocorrelation Γ, because the unknown phases are compensated by collecting coherent diffraction data from a plane at least twice as big as the sample. For higher oversampling O one can thus generalize Eq. 2.26 to

$$\xi_t > Oa. \tag{2.28}$$

For the temporal (longitudinal) coherence similar estimations can be made, i.e. two light rays originating from opposite sites of the sample should still interfere on the detector. Miao et al. empirically found [34] a relation between the bandwidth $\triangle\lambda$ of a light beam, the achievable resolution $\triangle r$ and the oversampling O:

$$\frac{\lambda}{\triangle\lambda} \geq \frac{Oa}{\triangle r} \Longrightarrow \triangle r \geq \frac{Oa\triangle\lambda}{\lambda}. \tag{2.29}$$

Hence the resolution is limited by the bandwidth,[6] i.e. the fringes smear out as was qualitatively already discussed in Sect. 2.2.1. At the same time one sees from Eqs. 2.28 and 2.29 that for a higher oversampling O one needs a higher temporal coherence, i.e. a smaller bandwidth $\triangle\lambda$, and a higher transverse coherence ξ_t. Since no additional resolution in the reconstruction is gained from higher oversampling, it can be concluded from this result to aim for $O \gtrsim 2$. If not avoidable, one can account for partial coherence in the phase retrieval algorithm (Sect. 2.3) [36].

If one now considers a diffraction experiment where the diffraction pattern is sampled on a regular N_x by N_y grid, one can assign every sampling point, i.e. each pixel, a corresponding sampling interval $\triangle q_x$ and $\triangle q_y$. The corresponding sampling interval of each single pixel at θ can be calculated using Eq. 2.23. From this one can deduce the field of view (FOV) in each axis to [28]

$$L_x = \frac{1}{\triangle q_x}, \qquad L_y = \frac{1}{\triangle q_y}. \tag{2.30}$$

At the same time the highest measured momentum transfer on the q_x-axis $q_{x,\max}$ results in the smallest resolvable period $\triangle r_x$ in the corresponding object plane axis[7]

$$\triangle r_x = \frac{1}{2q_{x,\max}}. \tag{2.31}$$

The same is of course valid for the q_y/y-axis and typically has the same result in a transmission CDI experiment where the detector is centered behind the sample. Hence, for a given detector width w and a detector sample distance z (see Fig. 2.5) one can determine the highest recorded scattering angles $\theta_{\max} = \tan^{-1}[w/(2z)]$ and use these to calculate the highest detectable momentum transfer as[8]

$$q_{\max} = \frac{2}{\lambda}\sin\left(\frac{\theta_{\max}}{2}\right) = \frac{2}{\lambda}\sin\left[\frac{1}{2}\tan^{-1}\left(\frac{w}{2z}\right)\right]. \tag{2.32}$$

[6] Provided that diffraction data is measured to sufficiently high momentum transfers, such that in principle a higher resolution could be obtained considering perfect coherence properties. See the following pages for the fundamental resolution limit.

[7] It is assumed that the zero deflection point, i.e. $|q| = 0$, resides in the center of the detector. The factor 2 comes from the fact that the pattern is sampled from $-[(N_x - 1)/2]\triangle q_x$ to $[N_x/2]\triangle q_x$ on the detector and that the FFT conserves the total amount of pixels, i.e. the object plane is also sampled by N_x times N_y pixels.

[8] This refers to the midpoints from the diagonal edges of the CCD. Sometimes in literature the highest momentum transfer in the edges of the detector is mentioned. It is thus a factor of $\sqrt{2}$ larger, but this yields no additional resolution because the highest momentum transfer with respect to the x- and y-axis is still the same.

Thus the smallest resolvable period becomes

$$\triangle r = \frac{\lambda}{4 \sin\left[\frac{1}{2}\tan^{-1}(\frac{w}{2z})\right]}. \tag{2.33}$$

For small angles $\theta_{\max}$ this compares to the well-known Abbe limit (Eq. 1.1), if $\mathrm{NA} = \sin[\tan^{-1}(\frac{w}{2z})]$ is considered as the numerical aperture of the system. Using the small angle approximation $\sin[\tan^{-1}(w/[2z])] \approx w/(2z)$ yields

$$\triangle r = \frac{z\lambda}{w} = \frac{z\lambda}{pN} = p_{\mathrm{obj}} \tag{2.34}$$

if a CCD having N pixels with a pixel width p is considered. Due to the principle of conservation of the number of pixels one can also interpret this as the pixel size p_{obj} in the object plane. This is also referred to as the *half-pitch distance* and it gives an estimate of the smallest details in an object that can be resolved provided the diffraction pattern can be measured with a sufficient signal to noise ratio at the edge of the detector.

2.3 Iterative Phase Retrieval Methods

In the previous sections diffraction of light waves on a sample was investigated and the phase problem (Sect. 2.2.3) was found, which needs to be solved in order to reconstruct the object. As pointed out by Sayre in 1952 [29], one can in principle solve the phase problem if oversampled diffraction patterns are measured. However, it took almost 20 years until Gerchberg and Saxton came up with a first algorithm [37] for the phase retrieval in a diffraction pattern, at this time for electron microscopes. In 1978 Fienup then introduced an improved version [38] of the Gerchberg-Saxton algorithm, which is known as the error-reduction algorithm. He introduced a support constraint, i.e. setting an area outside of the expected object to zero, and showed that this results in a more stable phase retrieval. Moreover, he introduced a positivity constraint, since a physical object's complex electron density cannot have a negative amplitude. The error-reduction algorithm, however, suffered from stagnation in local minima during the reconstruction and thus needed further improvement, which resulted in the hybrid input-output algorithm (HIO) [38]. In the HIO algorithm the amplitude that is projected outside of the support is used as an error, which one tries to reduce from iteration to iteration. The principal scheme for an iterative phase retrieval is depicted in Fig. 2.7. For the initialization of the algorithm (Fig. 2.7a) the measured amplitudes, i.e. $\sqrt{I(\mathbf{q})}$, and random phases are used. An initial support function S can be determined from the diffraction pattern if not otherwise known. This issue will be tackled later in this section.

The goal of the phase retrieval is to reconstruct the complex wave function $U(\mathbf{r})$, as discussed in Sect. 2.2.2, that is exiting the object plane. This is equivalent to

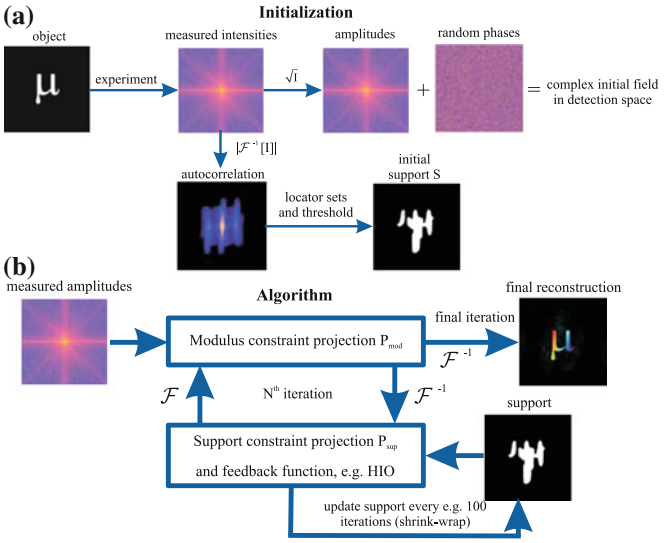

Fig. 2.7 Principal scheme for an iterative phase retrieval. **a** In a diffraction experiment one typically measures the intensities of the diffraction pattern in the far-field, i.e. the Fourier transform of the object. Since nothing is known about the phases one typically seeds the algorithm with random phases. From the modulus of the inverse Fourier transform of the measured intensities one obtains a function proportional to the autocorrelation, which can be used to obtain an initial support S that encloses the object. So-called locator sets can be used to enhance this first support estimate [39]. **b** After having seeded the algorithm as explained in (**a**) one iterates between detection plane and object plane using corresponding Fourier transforms. In the detection plane the modulus constraint is enforced, i.e. taking the measured amplitudes and keeping the phases. Likewise, in the object plane one enforces the support constraint by using a proper feedback function, which could for instance be the HIO formulation. The shrink-wrap method [40] is used to enhance the support every e.g. 100 iterations. The final reconstruction is depicted as complex-valued plane, where the hue and brightness encode the phase and amplitude, respectively. The linear phase ramp, visualized by the color transition in the final reconstruction, comes from a non-perfect centered diffraction pattern

reconstructing the object if one considers a coherent plane wave impinging on the object. In the detector plane one has the complex wave $\tilde{U}(\mathbf{q}) \propto \mathcal{F}[U(\mathbf{r})]$, from which one can only measure the intensity $I(\mathbf{q}) \propto \tilde{U}(\mathbf{q})\tilde{U}^*(\mathbf{q})$. Thus the modulus constraint (Fig. 2.7b) in the n-th iteration of the algorithm in the detector plane is defined as

$$\tilde{U}_{n+1}(\mathbf{q}) = \sqrt{I(\mathbf{q})}\exp[\mathrm{i}\arg\{\tilde{U}_n(\mathbf{q})\}], \tag{2.35}$$

i.e. one keeps the phases and replaces the amplitude by the square root of the measured intensities. Now one can think of the back transformation to the object plane as a projection, i.e. the modulus constraint projection, which is denoted as P_{mod}. This allows to write the modified wave function in the object plane in terms of the projection as

$$U_{n+1}(\mathbf{r}) = P_{\mathrm{mod}}U_n(\mathbf{r}) = \mathcal{F}^{-1}[\tilde{U}_{n+1}(\mathbf{q})]. \tag{2.36}$$

Next a projection in the object plane is applied, which is called the support projection P_{sup}. The support S is the region inside the object, i.e. surrounded by a zero-density region. One can write this projection as

$$P_{\text{sup}} U_{n+1}(\mathbf{r}) = \begin{cases} U_{n+1}(\mathbf{r}) & \in S \\ 0 & \notin S \end{cases}. \tag{2.37}$$

The beauty of these projections is that one can use them to write down a certain iterative algorithm in one formula. For instance the error-reduction algorithm can be written as

$$U_{n+1}(\mathbf{r}) = P_{\text{sup}} P_{\text{mod}} U_n(\mathbf{r}) \tag{2.38}$$

or the HIO as

$$U_{n+1}(\mathbf{r}) = \begin{cases} P_{\text{mod}} U_n(\mathbf{r}) & \in S \\ U_n(\mathbf{r}) - \beta P_{\text{mod}} U_n(\mathbf{r}) & \notin S \end{cases}, \tag{2.39}$$

where β is a feedback parameter with typical values between 0.1 and 1. Furthermore, sometimes additional constraints are enforced on the object plane. For example one can constrain that the object must be real-valued and positive $U_{n+1} \in \mathbb{R}^+$ in case of a non-absorbing aperture. In case of a pure phase-object one can use $U_{n+1} = \exp[\mathrm{i} \arg\{U_{n+1}\}]$ as an additional constraint. Even though this requires some knowledge about the object, it significantly decreases, if available, the search space for the algorithm and consequently speeds up the convergence. Over the years many different modifications to the HIO were introduced with each following a different goal. A comprehensive overview and comparison can be found in [40]. Mostly a mixture of algorithms is used within a reconstruction run, e.g. 100 iterations of HIO followed by a few error-reduction steps [28].

A realization of a noise-robust HIO dealing with noise[9] in the recorded diffraction pattern is presented in [41]. This realization was used for reconstructions in this thesis apart from the unmodified HIO. Another realization that was implemented and worked well on experimental data was Lukes relaxed averaged alternating reflection algorithm (RAAR) [42] which can be written as

$$U_{n+1}(\mathbf{r}) = \beta U_n(\mathbf{r}) + 2\beta P_{\text{sup}} P_{\text{mod}} U_n(\mathbf{r}) + (1 - 2\beta) P_{\text{mod}} U_n(\mathbf{r}) - \beta P_{\text{sup}} U_n(\mathbf{r}). \tag{2.40}$$

For all phase retrieval algorithms a tightly fitting support S is crucial. The support, however, is unknown in the general sense in microscopy. To get a first estimate of the support one can use that the autocorrelation of the object $o(\mathbf{r})$ is proportional to the inverse Fourier transform of the intensity diffraction pattern [39]

$$\Gamma(\mathbf{r}) = |\mathcal{F}^{-1}[I(\mathbf{q})]| \propto o(\mathbf{r}) \otimes o^*(-\mathbf{r}), \tag{2.41}$$

[9] Due to shot noise and electronic noise of the readout electronics.

which essentially means that one gets an outer bound for the object from the measured diffraction pattern. The autocorrelation can be practically thought of as translating the object $o(\mathbf{r})$ across itself in all directions and summing it up [39]. Hence the radius of the autocorrelation is always larger than the object. Using so-called *locator sets* [39], which basically use symmetries of the Fourier transform, one shifts $\Gamma(\mathbf{r})$ along a set of vectors and sums the resultant in a refined $\Gamma(\mathbf{r})$, see Fig. 2.7a. Proper thresholding of this refined $\Gamma(\mathbf{r})$ results in a support estimate S which is typically close to the actual object. Locator sets and the support determination from the autocorrelation will be used to reconstruct all objects in this thesis without any *a priori* knowledge.

Another important technique to improve the support during the iterations was introduced by Marchesini et al. and is known as the *shrink-wrap method* [43]. Shrink-wrap essentially updates the support after a given number of iterations based upon the current object plane reconstruction. In order to do this, one computes the modulus of the complex electron density in the object plane and applies a Gaussian filter and subsequently thresholds the result to determine a refined support. This method has proved to be very effective since it allows to get a tighter fit of the support to the actual object once the phases become more stable after a couple of iterations. It also helps to overcome the uncertainty of the first support estimation from the autocorrelation. Throughout this thesis shrink-wrap will be used for all reconstructions of experimental data. It is worth mentioning that an actual implementation of shrink-wrap introduces plenty of new parameters to the reconstruction, i.e. an amount of Gaussian blurring and the period of application. For most reconstructions in this thesis the Gaussian blurring is ramped down from e.g. 20 pixels standard deviation radius down to 1 and shrink-wrap is applied at about every 100th iteration.

When starting with random phases, one often finds deviating solutions in single HIO runs. Thus it is feasible to pick the best of the reconstructions after a certain number of iterations and average it with every other independent run and proceed further with the iterations. This technique is similar to genetic algorithms that are widely used for optimization problems [44]. In CDI this technique is termed *guided hybrid input-output* (GHIO) [45]. For some of the reconstructions in this thesis an implementation of GHIO was used. It worked well, especially if data is missing in the measured diffraction pattern, e.g. due to a beam stop that is used to block the bright central speckle.

The progress of the phase retrieval can be monitored by an appropriate error metric [46]. More important on the other hand is the success of the reconstruction in relation to the achieved resolution. As explained in Sect. 2.2.4 there is a fundamental resolution limitation set by the highest momentum transfer that can be measured. However, typically the magnitude of the signal in the Fourier domain decays quickly for increasing momentum transfer, thus in experiments the fringes measured at the edge of the CCD, if measured at all, are noisy. Hence, the resolution should be determined by the actual resolved diffraction pattern at the end of the phase retrieval, i.e. it should be checked what the highest momentum transfer that actually contributed to the reconstruction is. For this purpose Chapman et al. introduced the phase retrieval transfer function (PRTF) [28]

$$\mathrm{PRTF}(\mathbf{q}) = \frac{|<\tilde{U}_{\mathrm{final}}(\mathbf{q})\exp(\mathrm{i}\phi_0)>|}{\sqrt{I(\mathbf{q})}}, \tag{2.42}$$

where $\tilde{U}_{\mathrm{final}}(\mathbf{q})$ is the final complex-valued reconstructed field in the detector plane without applying the modulus constraint in the last step. The angle brackets denote averaging over several independent reconstruction runs for which one needs a multiplicative phase constant ϕ_0 to adjust the phase offset between the runs to a common level. The PRTF is then typically integrated over shells of constant $|\mathbf{q}|$ and plotted over $|\mathbf{q}|$. This function drops to zero if there is no relation between the averaged reconstructed amplitudes and the measured amplitudes, hence the PRTF can be extrapolated to zero in the drop-off region to determine the highest $|\mathbf{q}|$ that contributed to the reconstruction.[10] Using the formulas given in Sect. 2.2.4 one can then determine the achieved resolution.

2.4 Digital In-line Holography

The phase problem (Sect. 2.2.3) is the main limitation to directly assess an object from its diffraction pattern. Moreover, CDI as presented in the previous section is limited to isolated objects. A way to overcome this limitation is the use of a well-defined reference wave that causes interference fringes within the diffraction pattern, which are related to the local phase at the detector. Thus, if sufficiently highly sampled, one can retrieve the phase indirectly. This principle is well-known as holography and was pioneered by Gabor in the later 1940s [47], winning him the Nobel prize in 1971. Holography nowadays is a broad field with plenty of applications and possible geometries. A comprehensive overview is given in the book from Toal [48]. The first holographic X-ray measurements were carried out using synchrotron radiation [49, 50]. Over the years this technique was improved for instance by using resonances in the material to achieve selective imaging [51] or ultrafast temporally resolved holography [52]. Moreover, this technique can be used to characterize the incoming X-ray field if one considers a known object [53, 54]. The first digital in-line holography experiments with table-top HHG sources were carried out using the divergent wavefront after a focus [13] and later using pinhole references [55]. If the object is placed in a divergent beam, e.g. behind a focus, one can also get a mixture between holography and CDI, which is termed *Fresnel CDI* [25, 56, 57]. Most of the X-ray holography experiments, however, use a separate source for the reference wave, which is typically a small pinhole [51, 58], an array of references [59, 60] or an extended reference [61–63]. This is somewhat limiting, because the reference needs to be placed at a well-defined distance from the object in order to acquire a hologram that can be directly inverted by a single Fourier transform, which is then termed *Fourier transform holography* [51, 62].

[10] Alternatively, one can threshold the PRTF at e.g. 0.5 or $1/e$ to determine the highest $|q|$.

In the general case of unknown, e.g. biological samples, in-line holography allows to assess the sample. In in-line holography the reference wave is the same as the wave that is scattered at the object, i.e. the illumination wave, while only a part of this wave is influenced by the object. For XUV wavelengths Gabor in-line holography was successfully used to write the hologram into PMMA for later analysis [64]. More practical in terms of microscopy is, however, digital in-line holography [65–67], where a detector captures the hologram and a computer carries out the reconstruction of an object image [68, 69]. From now on, the discussion in this thesis will be limited to digital in-line holography (DIH) only, since this type of holography was used for experiments in this work (Sect. 3.3).

The notation and discussion will follow an excellent overview given by Garcia-Sucerquia et al. [70]. In CDI one considers a plane wave impinging on the object causing a diffraction pattern. Since a plane wave in Gaussian optics can be attributed to a beam having infinitely low divergence, one can, according to the Huygens-Fresnel principle, only capture a diffraction pattern in the far-field caused by interference of wavelets emitted from different parts of the object (Fig. 2.8a, b). In DIH however, one expects a spherical wave, for sample illumination as well as for serving as reference, $U_{\mathrm{ref}}(\mathbf{r}) = \exp(\mathrm{i}\mathbf{kr})/r$ arriving at the object. Since the spherical pinhole wavefronts have a divergence similar to the object wavefronts, an interference pattern from the reference wave $U_{\mathrm{ref}}(\mathbf{r})$ and the scattered wave $U_{\mathrm{scat}}(\mathbf{r})$ forms in the detector plane (Fig. 2.8c). From the field $U_{\mathrm{det}}(\mathbf{r})$ in the detection plane one can only record the intensities, which can be written as

$$\begin{aligned} I(\mathbf{r}) = |U_{\mathrm{det}}(\mathbf{r})|^2 &= |U_{\mathrm{ref}}(\mathbf{r}) + U_{\mathrm{scat}}(\mathbf{r})|^2 \\ &= [U^*_{\mathrm{ref}}(\mathbf{r})U_{\mathrm{scat}}(\mathbf{r}) + U_{\mathrm{ref}}(\mathbf{r})U^*_{\mathrm{scat}}(\mathbf{r})] \\ &\quad + |U_{\mathrm{scat}}(\mathbf{r})|^2 + |U_{\mathrm{ref}}(\mathbf{r})|^2. \end{aligned} \tag{2.43}$$

Inspecting the terms in Eq. 2.43 one finds the interference between the scattered and the reference wave in the first term (in the brackets), which gives rise to the hologram (Fig. 2.8d). The diffraction pattern analogue to CDI can be found in the second term. The third term is the far-field of the source, which, in case of a small point-like source, is just a constant field that could be subtracted. Hence for DIH it is essential that the object does not entirely block the reference wave. However, even for apertures DIH works, but the fringe contrast is getting worse the more of the reference is blocked by an opaque object [70]. Moreover, the geometry of DIH is dictated by the source size, i.e. the divergence of the reference beam. If a pinhole is used for illuminating an object care must be taken that the zeroth order of the produced Airy pattern[11] covers both the object and the detector in order to get a well resolved hologram. Comparing Fig. 2.8b, d reveals an important advantage of in-line holography, which is that in DIH no beam block is needed to suppress the central high intensity maximum as it occurs in CDI. Moreover the intensity distribution across the

[11] An *Airy pattern* or *Airy disk* is the diffraction pattern caused from a round aperture featuring a bright central maximum, i.e. zeroth diffraction order, surrounded by dark and bright rings, i.e. higher order diffraction terms.

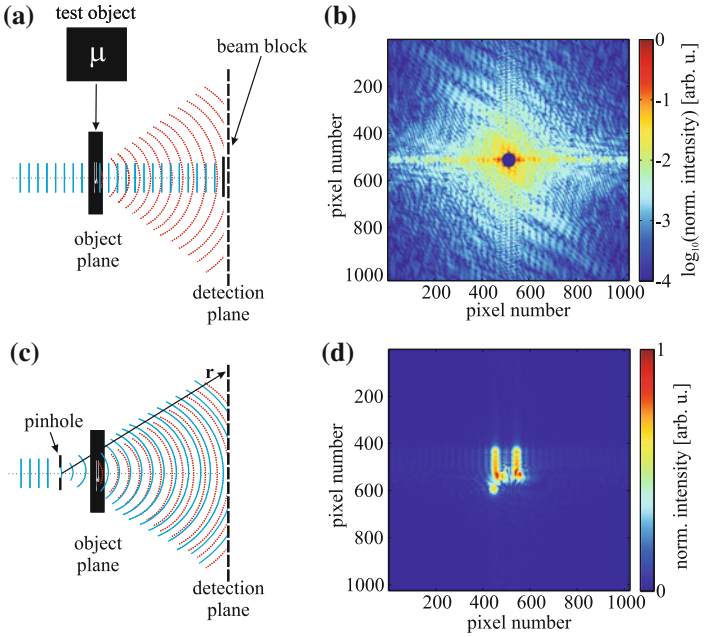

Fig. 2.8 Comparison of CDI and DIH with a μ-shaped aperture. **a** In a CDI configuration the object is illuminated with a plane wave (*solid blue line*), which can partly propagate through the aperture and partly gives rise to the diffracted wave (*red dotted line*). Through Babinet's principle one can also think of a μ-shaped object in free space, where part of the impinging wave far away from the object propagates undisturbed to the detector. Typically, a beam stop is used to suppress the bright central speckle in order to have a better use of the limited dynamic range of the detector. **b** The intensity of the diffraction pattern (logarithmic scale) caused by the object. **c** A pinhole is placed in front of the object in order to illuminate it with a spherical wave. Thus one has the reference wave (*solid blue line*) and the diffracted (object) wave (*dotted red line*) covering the detector causing interferences across the detector. This is a typical DIH setup. **d** A simulated hologram one would measure in the far-field of a 40 µm large μ-shaped aperture that is illuminated with a 1 µm pinhole 1.9 mm away with $\lambda = 38$ nm wavelength. Please note that the intensity scale in (**d**) is linear

detector is homogeneous compared to CDI diffraction patterns where the intensities of the fringes typically vary by several orders of magnitude across the detector. This is expressed by the logarithmic intensity scale in Fig. 2.8b and the linear intensity scale in Fig. 2.8d. Another consequence is that noise in the measurement of a hologram has much less effect compared to CDI, because small fluctuations contribute less to the overall result. A much more detailed theoretical analysis of DIH can for instance be found in the thesis from Schürmann [71].

In Chap. 3 the setup that was used for DIH in this work is introduced. In a nutshell it consists of a pinhole having a certain diameter that is placed in the focus of a monochromatized HHG beam. This pinhole generates the spherical illumination wave, which is then diffracted at the object. The undisturbed part of this wave propagates to the detector and further serves as reference wave. In the far-field a CCD records the hologram. An excellent book from Poon and Banerjee [72] covers

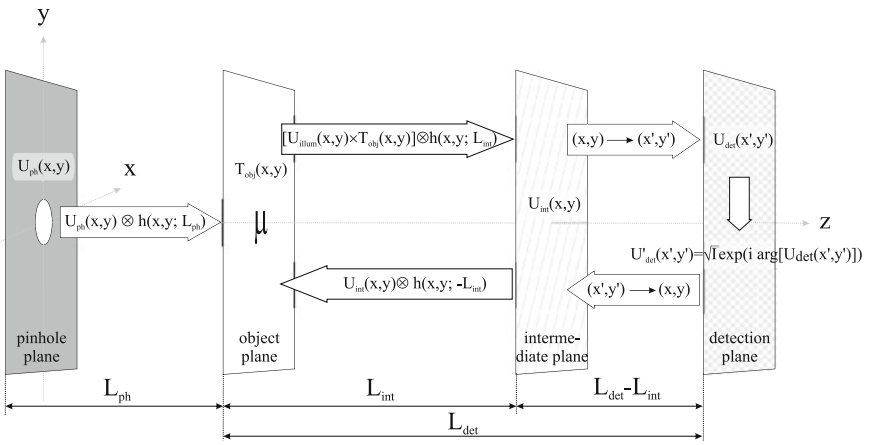

Fig. 2.9 Reconstruction scheme for the digital in-line holograms as used in this thesis. The convolution ($\otimes$) of the Fresnel propagator $h(x, y; z)$ with an input field $U(x, y)$ was used to propagate the field between the planes. Starting at the pinhole plane one propagates the field to the object plane, where the field is multiplied with an in general complex-valued transmission function of the object $T_{\text{obj}}(x, y)$. Then the field is propagated to the far-field given at an intermediate plane, see text for detailed explanation. A coordinate transform scales the field to the detector where the phases are kept and the measured amplitudes $\sqrt{I}$ are enforced. After back propagation to the object plane the object function is updated. These steps are repeated until convergence

this topic and its numerical integration in depth. Here, some of the notations given there will be used for the reconstruction. In order to reconstruct these holograms the following procedure is used (Fig. 2.9):

1. One starts in the pinhole plane with a field $U_{\text{ph}}(x, y)$ that has a flat phase and a radial distribution.
2. According to Chap. 3 in [72] one can compute the Fresnel diffraction pattern after a distance z (see Fig. 2.4), by convoluting the input field $U_{\text{ph}}(x, y)$ with the spatial impulse response $h(x, y; z)$

$$h(x, y; z) = \exp(-\mathrm{i}kz)\frac{\mathrm{i}k}{2\pi z}\exp\left[-\mathrm{i}k\frac{(x^2 + y^2)}{2z}\right], \tag{2.44}$$

also known as the *Fresnel propagator*. The numerical implementation can be done by Fourier transforming the propagator h and the field U, multiplying them in Fourier space and Fourier transforming the result back, i.e.

$$U(x, y)\big|_z = \alpha\mathcal{F}^{-1}\{\mathcal{F}[h(x, y; z)] \times \mathcal{F}[U(x, y)]\}, \tag{2.45}$$

where α is a constant scale factor depending on the actual implementation of the FFT algorithm. Using this, the illumination field at the object plane can be computed by $U_{\text{illum}}(x, y) = U_{\text{ph}} \otimes h(x, y; L_{\text{ph}})$ when the pinhole plane and

object plane are L_{ph} apart. This is essentially an Airy pattern. The experiment is aligned such that the zeroth order of the pattern, which contains 84 % of the energy, fits to the sample.

3. Now, in the object plane, one multiplies $U_{\mathrm{illum}}(x, y)$ with the transmission function of the object $T_{\mathrm{obj}}(x, y)$, which could e. g. be a simple step-function having the spatial shape of the object if one considers an opaque aperture. From this one gets the object plane exit wave $U_{\mathrm{obj}}(x, y) = U_{\mathrm{illum}}(x, y) \times T_{\mathrm{obj}}(x, y)$.
4. $U_{\mathrm{obj}}(x, y)$ is then propagated to the far-field, which is an intermediate plane $U_{\mathrm{int}}(x, y)$ a couple of Fresnel lengths (Eq. 2.12) behind the object plane. Due to the large divergence of the beam the field spreads quickly spatially, which would demand a large computation grid to sufficiently sample amplitude and phase on the full propagation distance to the detector. Thus, the wave is just propagated a short distance L_{int} to be safely in the far-field regime. As explained earlier in Sect. 2.2.2 the diffraction pattern, or hologram in this case, only spreads spatially when propagating further but does not change its shape. Hence one can use a coordinate transformation $(x \rightarrow x', y \rightarrow y')$ to transform the intermediate plane to the actual detector plane and get $U_{\mathrm{det}}(x', y')$. The coordinate transform is applied in order to have sufficient sampling at the object plane, while keeping the computation space maintainable. This procedure is illustrated in more detail in [67].
5. In the detector plane, methods inspired by the HIO algorithm (Sect. 2.3) are used, i.e. keeping the phases of $U_{\mathrm{det}}(x', y')$ and replace the amplitudes with the square root of the measured intensities.
6. Then the wave is transformed back to the intermediate plane, i.e. $(x' \rightarrow x, y' \rightarrow y)$, and propagated back to the object plane to get a new $U'_{\mathrm{obj}}(x, y)$. Now a new estimate of the object transmission $T'_{\mathrm{obj}}(x, y) = U'_{\mathrm{obj}}(x, y) - U_{\mathrm{illum}}(x, y)$ is calculated.[12]

Steps 3–6 are now iteratively repeated until convergence occurs. It is worth noting that there is some similarity to the algorithm described in [67], with the differences mainly being that here a convolution of the Fresnel propagator is used instead of analytical formulas. This severely speeds up the computation, because, as outlined above, the convolution can be done by using FFTs, which in turn can be effectively parallelized. Moreover, here the full system is computed starting from the source producing an illumination wave. Hence, in contrast to the algorithm reported in [67], there is no limitation to real objects, since here $T_{\mathrm{obj}}(x, y)$ could in general be complex-valued, e.g. for partly transparent objects that would change phase and amplitude of the illuminating wave. Further, it can be used to determine the illumination field in great detail if a known object, e.g. a rectangular aperture, is enforced and one loops through

[12] Other iterative methods reported in literature make use of the Gerchberg-Saxton algorithm [73] or use a support constraint to retrieve the hologram [74, 75]. The important difference is that here the full illumination field, which is well characterized by the pinhole being illuminated with a XUV beam having good coherence properties, is used at every step, in contrast to the algorithms reported in literature, which mostly switch between the object plane and the detector plane and disregard the illumination field.

all the steps. It also proved to work successfully for samples that are mostly consisting of strongly absorbing regions to use $T_{\text{obj}}(x, y)$ just as a binary function determined by the shrink-wrap method analogous to the support function S in the HIO algorithm and then calculate the complex-valued sample in the final iteration of the algorithm by

$$U_{\text{sample}} = U_{\text{int}}(x, y) \otimes h(x, y; -L_{\text{int}}) - U_{\text{illum}}. \tag{2.46}$$

The idea behind this is that all hard edges caused by opaque parts of the object cause intense fringes and likely dominate the hologram. Hence the rough structure of the object is enforced first and the partially transparent parts are recovered in the final step. In the results in Sect. 4.1, samples that justify this approach will be presented.

It is worth noting that the holographic procedure offers the possibility of reconstructing the object in an arbitrary plane using one hologram. Thus in principle three-dimensional information about the object can be retrieved to a certain extent by refocussing to different planes [70]. Moreover, the quality of the reconstruction can be enhanced by measuring the amplitude of the reference wave and then using this as an illumination field instead of the numerically produced illumination field discussed in this section.

The resolution, as was discussed in the previous sections, depends on the numerical aperture according to Eq. 1.1. For digital in-line holography using spherical waves the NA is [70]

$$\text{NA} = \frac{w}{2\sqrt{\left(\frac{w}{2}\right)^2 + L_{\text{det}}^2}}, \tag{2.47}$$

where w is the width of the detector. The NA is obviously independent of the source size, however, as discussed earlier in this section one needs a homogeneous illumination by employing the central maximum of the Airy pattern produced by the pinhole. The angular radius θ_0 of the first dark ring of an Airy pattern is given by

$$\sin\theta_0 = 1.22\frac{\lambda}{a}, \tag{2.48}$$

where a is the diameter of the aperture. The small angle approximation $\sin\theta_0 \approx \tan\theta_0$ is almost always justified in DIH experiments. Hence, one can calculate the approximate diameter of the central maximum of the Airy disk on the detector placed at L_{det}[13]

$$w_{\text{Airy}} = 2 \cdot 1.22\frac{\lambda}{a}L_{\text{det}}. \tag{2.49}$$

Physically this means that one observes a larger central maximum for a smaller pinhole if the detector is kept at constant distance. If $w_{\text{Airy}} < w$ and if the higher order

[13] More precisely it would be $L_{\text{det}} + L_{\text{ph}}$, however, for all experiments presented in this thesis $L_{\text{det}} \gg L_{\text{ph}}$, hence simply L_{det} is used.

maxima of the Airy pattern are neglected one can calculate an effective numerical aperture of the system

$$\mathrm{NA}_{\mathrm{eff}} = \frac{1.22\frac{\lambda}{a}L_{\mathrm{det}}}{\sqrt{\left(1.22\frac{\lambda}{a}L_{\mathrm{det}}\right)^2 + L_{\mathrm{det}}^2}} = \frac{1}{\sqrt{1 + 0.67\frac{a^2}{\lambda^2}}}, \tag{2.50}$$

which now is obviously only dependent on the pinhole size and the wavelength. For XUV DIH usually $a \gg \lambda$, which allows to simplify Eq. 2.50 to $\mathrm{NA}_{\mathrm{eff}} \approx \frac{1.22\lambda}{a}$. The practical implication of this result is that one should match the pinhole size to the dimensions of the detector and its anticipated distance [76]. In this case one can compute the NA and thus the achievable resolution simply by Eq. 2.47. Of course one could argue to use a pinhole so tiny that $w_{\mathrm{Airy}} \gg w$ is always fulfilled. However, in table-top HHG experiments the XUV flux is not excessive and thus best use of the available photons should be made. Hence, it can be concluded that it is beneficial to choose a pinhole that fits the detector and its achievable distance from the pinhole in order to realize the best performance in terms of the photon flux and the achievable resolution. In view of maximizing the magnification ζ

$$\zeta = L_{\mathrm{det}}/L_{\mathrm{ph}}, \tag{2.51}$$

which is inferred from the intercept theorem, one has to place the sample as close to the pinhole as mechanically possible.[14] On the other hand the field of view is minimized in this case. If the distance between sample and pinhole is too large, one cannot resolve the fringes if the Shannon-Nyquist theorem is violated. Hence, the optimal position of the sample relative to the pinhole and the CCD is somewhere in between and should be set such that the period of the smallest fringes is in the range of e.g. 5–10 pixels on the CCD [77]. In that case the FOV and object space NA, and thus the achievable resolution, are optimal.

If, however, $L_{\mathrm{det}} \gg L_{\mathrm{ph}}$, i.e. when the object is close to the pinhole, one could think of a spherical particle in the object plane at approximately the distance of the pinhole. To have a resolvable fringe one needs to have at least the first ring of the Airy pattern produced by the particle on the detector,[15] hence the discussion is exactly the same as above for the pinhole. For example, if one thinks of a 1 µm pinhole as the reference source and a round particle of e.g. 500 nm diameter in the object plane one will not observe any fringe from that particle on the detector because the emission cone of its partial wave is coarser than the one from the pinhole. In terms of the back projection this means that one cannot resolve this particle. The conclusion from this discussion is that the size of the pinhole is not just limiting the effective NA but also the resolution itself. As a rule of thumb it can be summarized that a resolution of approximately the size of the pinhole is achievable.

[14] For typical XUV wavelengths and pinhole sizes in the order of a micron the Fraunhofer condition (Eq. 2.12) is already fulfilled a few tens of microns behind the pinhole. Hence, the Fraunhofer condition is not limiting in XUV DIH.

[15] This is analogous to the Rayleigh criterion.

2.5 CDI State-of-the-Art and Chapter Summary

The CDI technique presented in the fundamentals chapter allows imaging of isolated objects at the nanometer scale without the use of imaging optics. This renders those systems very compact. In the case of table-top CDI experiments, the whole apparatus can fit on an optical table of a few square meters. Another major benefit is that lossy optical elements, such as Fresnel zone plates, are avoided. Moreover, the mechanical stability of the imaging system is less important, because lateral shifts of the object would only affect the phase in the far-field (Fourier space), which in any case cannot be measured. This is quite astonishing if one considers achieving a few nanometers of resolution while the mechanical stability of the system only needs to ensure that the beam homogeneously overlaps with the object during exposure. If one would use imaging optics instead, one would need a mechanical stability comparable to the desired resolution, which can be very challenging if nanometer resolution is aimed for. One major drawback of CDI, however, is that so far only isolated objects were considered, which could be e.g. an isolated cell, a structured aperture or a sample on a fixed support frame. It was demonstrated that digital in-line holography can be used to solve this problem at the expense of introducing another reference wave forming object, e.g. a pinhole. The latter will typically limit the achievable flux of the source and dictate the geometry of the imaging system. Moreover, the mechanical stability issue described above arises.

In recent years a technique called *ptychography* was developed, which overcomes this drawback [78, 79]. Ptychography uses a set of diffraction patterns obtained from an extended object, where the illuminated region is shifted from one exposure to the next while each exposure region overlaps with the previous. This produces a set of overdetermined diffraction patterns, which can then again be used to reconstruct the whole object plane. An extension of ptychography is called *keyhole diffraction imaging* [80] which is a combination of curved beam illumination at high numerical apertures, i.e. in-line holography combined with CDI, with ptychographic scanning. The latter technique shows quicker convergence behavior compared to pure ptychography. It is worth noting that the drawback of these techniques is again the need for high mechanical stability and limitations imposed by tight focusing optics, which currently restricts the application to synchrotrons and free-electron laser sources.[16] However, very recently first results on ptychography using table-top sources were published [81, 82].

Over the last decade the general field of CDI developed rapidly at synchrotrons and later at free-electron lasers. From its first experimental demonstration [83] it went on to image biological specimens such as single cells [84, 85] at a resolution of a few nanometers. An important improvement was introduced by Raines and co-workers who found that one can even extract three-dimensional data from a single diffraction pattern [86] if it is captured at a high numerical aperture. Other realizations of full 3D imaging combine tomographic techniques with CDI [28, 87]. The next goal

[16] This is because the high flux of such sources allows extremely short exposures down to single shot measurements which circumvents the stability problem.

that is to be achieved with novel free-electron laser sources, such as the EUROPEAN XFEL project, is atomic resolution, i.e. $\triangle r < 0.1\,\text{nm}$. The major problem faced here is that the photon energies necessary to achieve this resolution in principle are so high that matter is destroyed already after one exposure [88–90]. Hence, only single shot exposures can be used. However, for atomic resolution $>10^{14}$ photons/μm^2 in a single pulse would be necessary to get a sufficient signal in the diffraction pattern [91]. These numbers are out of reach for current FEL machines. Hence atomic resolution is one of the major goals for the coming years in CDI. In the meantime averaging over diffraction patterns obtained from replicas of the same objects was proposed [92] and demonstrated [93, 94] for proteins. Additional contrast is obtained by growing the protein as a crystal to get a macroscopic diffraction pattern of the same protein. Molecular reconstruction techniques are then used to fit the molecular structure to the diffraction pattern [93]. These techniques include the full three-dimensional reconstruction of the object.

Broad usage of CDI in all fields of science and especially for medical application is not feasible at next-generation synchrotrons and free-electron lasers, because such large scale facilities have limited access and are expensive to operate. An alternative are HHG sources that offer excellent XUV beams [13, 14] in terms of coherence allowing for table-top CDI experiments. Limiting is the flux in terms of exposure time and the bandwidth of the harmonics (cf. Eq. 2.29), and the achievable wavelengths in terms of resolution. Table-top CDI was first demonstrated by Sandberg et al. [95], while first holography measurements were done by Bartels et al. [13]. Abbey et al. demonstrated that the limitation due to bandwidth can be overcome for sufficiently discrete structures [96]. Likewise this can be applied to the harmonics frequency comb [97], while one has to keep in mind that this may work only for discrete objects that generate a limited amount of fringes such that the fringes caused by different harmonics are not overlapping. However, if this condition is fulfilled one can take advantage of the improved overall flux. Using more powerful laser sources even single shot HHG imaging was demonstrated [98, 99]. The flux from typical HHG sources does not endanger the detector unlike at FELs, hence the detector can be placed very close to the sample to achieve a high numerical aperture to take full advantage of the short wavelength radiation. Using a high numerical aperture in a table-top XUV experiment a resolution of 22 nm was achieved using 13.5 nm wavelength [100] which equals 1.6λ. It is also worth mentioning that HHG offers very short XUV bursts in the range of attoseconds to femtoseconds with the availability of a time-locked infrared laser, thus offering perfect capabilities for time resolved measurements [101, 102].

References

1. Boyd, R.W.: Nonlinear Optics. Academic Press, London (2008)
2. Schaefer, C., Niedrig, H., Bergmann, L., Eichler, H.-J.: Lehrbuch der Experimentalphysik. Walter de Gruyter, Berlin (2004) (Optik)

3. McPherson, A., Gibson, G., Jara, H., Johann, U., Luk, T.S., Mcintyre, I.A., Boyer, K., Rhodes, C.K.: Studies of multiphoton production of vacuum ultraviolet-radiation in the rare-gases. J. Opt. Soc. Am. B **4**(4), 595–601 (1987)
4. Li, X.F., L'Huillier, A., Ferray, M., Lompre, L.A., Mainfray, G.: Multiple-harmonic generation in rare gases at high laser intensity. Phys. Rev. A **39**(11), 5751–5761 (1989)
5. Seres, J., Seres, E., Verhoef, A.J., Tempea, G., Streli, C., Wobrauschek, P., Yakovlev, V., Scrinzi, A., Spielmann, C., Krausz, F.: Laser technology: source of coherent kiloelectronvolt X-rays. Nature **433**(7026), 596–596 (2005)
6. Popmintchev, T., Chen, M.C., Popmintchev, D., Arpin, P., Brown, S., Alisauskas, S., Andriukaitis, G., Balciunas, T., Mucke, O.D., Pugzlys, A., Baltuska, A., Shim, B., Schrauth, S.E., Gaeta, A., Hernandez-Garcia, C., Plaja, L., Becker, A., Jaron-Becker, A., Murnane, M.M., Kapteyn, H.C.: Bright coherent ultrahigh harmonics in the keV X-ray regime from mid-infrared femtosecond lasers. Science **336**(6086), 1287–1291 (2012)
7. Krause, J.L., Schafer, K.J., Kulander, K.C.: High-order harmonic generation from atoms and ions in the high intensity regime. Phys. Rev. Lett. **68**(24), 3535–3538 (1992)
8. Corkum, P.B.: Plasma perspective on strong field multiphoton ionization. Phys. Rev. Lett. **71**(13), 1994–1997 (1993)
9. Awasthi, M., Vanne, Y.V., Saenz, A., Castro, A., Decleva, P.: Single-active-electron approximation for describing molecules in ultrashort laser pulses and its application to molecular hydrogen. Phys. Rev. A **77**(6), 063403 (2008)
10. Keldysh, L.V.: Ionization in field of a strong electromagnetic wave. Sov. Phys. JETP **20**(5), 1307–1314 (1965)
11. Brabec, T., Krausz, F.: Intense few-cycle laser fields: frontiers of nonlinear optics. Rev. Mod. Phys. **72**(2), 545–591 (2000)
12. Lewenstein, M., Balcou, Ph, Ivanov, M.Y., L'Huillier, A., Corkum, P.B.: Theory of high-harmonic generation by low-frequency laser fields. Phys. Rev. A **49**(3), 2117–2132 (1994)
13. Bartels, R.A., Paul, A., Green, H., Kapteyn, H.C., Murnane, M.M., Backus, S., Christov, I.P., Liu, Y.W., Attwood, D., Jacobsen, C.: Generation of spatially coherent light at extreme ultraviolet wavelengths. Science **297**(5580), 376–378 (2002)
14. Ditmire, T., Gumbrell, E.T., Smith, R.A., Tisch, J.W.G., Meyerhofer, D.D., Hutchinson, M.H.R.: Spatial coherence measurement of soft X-ray radiation produced by high order harmonic generation. Phys. Rev. Lett. **77**(23), 4756–4759 (1996)
15. Constant, E., Garzella, D., Breger, P., Mevel, E., Dorrer, C., Le Blanc, C., Salin, F., Agostini, P.: Optimizing high harmonic generation in absorbing gases: model and experiment. Phys. Rev. Lett. **82**(8), 1668–1671 (1999)
16. Takahashi, E., Nabekawa, Y., Midorikawa, K.: Generation of 10-μJ coherent extreme-ultraviolet light by use of high-order harmonics. Opt. Lett. **27**(21), 1920–1922 (2002)
17. Popmintchev, T., Chen, M.C., Bahabad, A., Gerrity, M., Sidorenko, P., Cohen, O., Christov, I.P., Murnane, M.M., Kapteyn, H.C.: Phase matching of high harmonic generation in the soft and hard X-ray regions of the spectrum. Proc. Natl. Acad. Sci. USA **106**(26), 10516–10521 (2009)
18. Paul, P.M., Toma, E.S., Breger, P., Mullot, G., Auge, F., Balcou, Ph., Muller, H.G., Agostini, P.: Observation of a train of attosecond pulses from high harmonic generation. Science **292**(5522), 1689–1692 (2001)
19. Myers, O.E.: Studies of transmission zone plates. Am. J. Phys. **19**(6), 359–365 (1951)
20. Horowitz, P.: Scanning X-ray microscope using synchrotron radiation. Science **178**(4061), 608–611 (1972)
21. Lee, K.H., Park, S.B., Singhal, H., Nam, C.H.: Ultrafast direct imaging using a single high harmonic burst. Opt. Lett. **38**(8), 1253–1255 (2013)
22. Attwood, D.: Soft X-rays and Extreme Ultraviolet Radiation: Principles and Applications. Cambridge University Press, Cambridge (2007)
23. Jackson, J.D., Witte, C., Mueller, K.: Klassische Elektrodynamik, vol. 3. Walter de Gruyter, Berlin (2006)
24. Gu, M.: Advanced Optical Imaging Theory. Springer, Berlin (2000)

25. Williams, G.J., Quiney, H.M., Dhal, B.B., Tran, C.Q., Nugent, K.A., Peele, A.G., Paterson, D., de Jonge, M.D.: Fresnel coherent diffractive imaging. Phys. Rev. Lett. **97**(2), 025506 (2006)
26. Consortini, A.: Trends in Optics: Research, Developments, and Applications. Academic Press, London (1996)
27. Ewald, P.P.: Zur Theorie der Interferenzen der Roentgenstrahlen in Kristallen. Phys. Zeitschrift **14**, 465–472 (1913)
28. Chapman, H.N., Barty, A., Marchesini, S., Noy, A., Hau-Riege, S.P., Cui, C., Howells, M.R., Rosen, R., He, H., Spence, J.C., Weierstall, U., Beetz, T., Jacobsen, C., Shapiro, D.: High-resolution ab initio three-dimensional X-ray diffraction microscopy. J. Opt. Soc. Am. A Opt. Image Sci. Vis. **23**(5), 1179–1200 (2006)
29. Sayre, D.: Some Implications of a theorem due to shannon. Acta Crystallogr. **5**(6), 843–843 (1952)
30. Shannon, C.E.: Communication in the presence of noise. Proc. IRE **37**(1), 10–21 (1949)
31. Sayre, D.: Prospects for long-wavelength X-ray microscopy and diffraction. In: Schlenker, M., Fink, M., Goedgebuer, J.P., Malgrange, C., Vieenot, J.C., Wade, R.H. (eds.) Imaging Processes and Coherence in Physics, vol. 112, pp. 229–235. Springer, Berlin (1980)
32. Bates, R.H.T.: Fourier phase problems are uniquely solvable in more than one dimension. I: underlying theory. Optik **61**, 247–262 (1982)
33. Miao, J., Sayre, D.: On possible extensions of X-ray crystallography through diffraction-pattern oversampling. Acta Crystallogr. A **56**(6), 596–605 (2000)
34. Miao, J., Ishikawa, T., Anderson, E.H., Hodgson, K.O.: Phase retrieval of diffraction patterns from noncrystalline samples using the oversampling method. Phys. Rev. B **67**(17), 174104 (2003)
35. Spence, J.C., Weierstall, U., Howells, M.: Coherence and sampling requirements for diffractive imaging. Ultramicroscopy **101**(2–4), 149–152 (2004)
36. Whitehead, L.W., Williams, G.J., Quiney, H.M., Vine, D.J., Dilanian, R.A., Flewett, S., Nugent, K.A., Peele, A.G. Balaur, E. McNulty, I.: Diffractive imaging using partially coherent X-rays. Phys. Rev. Lett. **103**(24), 243902 (2009)
37. Gerchberg, R.W., Saxton, W.O.: Phase determination from image and diffraction plane pictures in electron-microscope. Optik **34**(3), 275–283 (1971)
38. Fienup, J.R.: Phase retrieval algorithms: a comparison. Appl. Opt. **21**(15), 2758–2769 (1982)
39. Fienup, J.R., Crimmins, T.R., Holsztynski, W.: Reconstruction of the support of an object from the support of its auto-correlation. J. Opt. Soc. Am. **72**(5), 610–624 (1982)
40. Marchesini, S., Chapman, H.N., Hau-Riege, S.P., London, R.A., Szoke, A., He, H., Howells, M.R., Padmore, H., Rosen, R., Spence, J.C.H., Weierstall, U.: Coherent X-ray diffractive imaging: applications and limitations. Opt. Express **11**(19), 2344–2353 (2003)
41. Martin, A.V., Wang, F., Loh, N.D., Ekeberg, T., Maia, F.R.N.C., Hantke, M., van der Schot, G., Hampton, C.Y., Sierra, R.G., Aquila, A., Bajt, S., Barthelmess, M., Bostedt, C., Bozek, J.D., Coppola, N., Epp, S.W., Erk, B., Fleckenstein, H., Foucar, L., Frank, M., Graafsma, H., Gumprecht, L., Hartmann, A., Hartmann, R., Hauser, G., Hirsemann, H., Holl, P., Kassemeyer, S., Kimmel, N., Liang, M., Lomb, L., Marchesini, S., Nass, K., Pedersoli, E., Reich, C., Rolles, D., Rudek, B., Rudenko, A., Schulz, J., Shoeman, R.L., Soltau, H., Starodub, D., Steinbrener, J., Stellato, F., Strueder, L., Ullrich, J., Weidenspointner, G., White, T.A., Wunderer, C.B., Barty, A., Schlichting, I., Bogan, M.J., Chapman, H.N.: Noise-robust coherent diffractive imaging with a single diffraction pattern. Opt. Express **20**(15), 16650–16661 (2012)
42. Luke, D.R.: Relaxed averaged alternating reflections for diffraction imaging. Inverse Prob. **21**(1), 37–50 (2005)
43. Marchesini, S., He, H., Chapman, H.N., Hau-Riege, S.P., Noy, A., Howells, M.R., Weierstall, U., Spence, J.C.H.: X-ray image reconstruction from a diffraction pattern alone. Phys. Rev. B **68**(14), 140101 (2003)
44. Baeck, T., Schwefel, H.-P.: An overview of evolutionary algorithms for parameter optimization. Evol. Comput. **1**(1), 1–23 (1993)

45. Miao, J., Chen, C.-C., Song, C., Nishino, Y., Kohmura, Y., Ishikawa, T., Ramunno-Johnson, D., Lee, T.-K., Risbud, S.H.: Three-dimensional GaN-Ga_2O_3 core shell structure revealed by X-ray diffraction microscopy. Phys. Rev. Lett. **97**(21), 215503 (2006)
46. Miao, J., Sayre, D., Chapman, H.N.: Phase retrieval from the magnitude of the Fourier transforms of nonperiodic objects. J. Opt. Soc. Am. A **15**(6), 1662–1669 (1998)
47. Gabor, D.: Microscopy by reconstructed wave-fronts. Proc. R. Soc. Lon. Ser. A **197**(1051), 454–487 (1949)
48. Toal, V.: Introduction to Holography. CRC Press, Boca Raton (2011)
49. Howells, M., Jacobsen, C., Kirz, J., Feder, R., Mcquaid, K., Rothman, S.: X-ray holograms at improved resolution—a study of Zymogen Granules. Science **238**(4826), 514–517 (1987)
50. McNulty, I., Kirz, J., Jacobsen, C., Anderson, E.H., Howells, M.R., Kern, D.P.: High-resolution imaging by Fourier transform X-ray holography. Science **256**(5059), 1009–1012 (1992)
51. Eisebitt, S., Luning, J., Schlotter, W.F., Lorgen, M., Hellwig, O., Eberhardt, W., Stohr, J.: Lensless imaging of magnetic nanostructures by X-ray spectro-holography. Nature **432**(7019), 885–888 (2004)
52. Chapman, H.N., Hau-Riege, S.P., Bogan, M.J., Bajt, S., Barty, A., Boutet, S., Marchesini, S., Frank, M., Woods, B.W., Benner, W.H., London, R.A., Rohner, U., Szoke, A., Spiller, E., Moller, T., Bostedt, C., Shapiro, D.A., Kuhlmann, M., Treusch, R., Plonjes, E., Burmeister, F., Bergh, M., Caleman, C., Huldt, G., Seibert, M.M., Hajdu, J.: Femtosecond time-delay X-ray holography. Nature **448**(7154), 676–679 (2007)
53. Quiney, H.M., Peele, A.G., Cai, Z., Paterson, D., Nugent, K.A.: Diffractive imaging of highly focused X-ray fields. Nat. Phys. **2**(2), 101–104 (2006)
54. Schropp, A., Hoppe, R., Meier, V., Patommel, J., Seiboth, F., Lee, H.J., Nagler, B., Galtier, E.C., Arnold, B., Zastrau, U., Hastings, J.B., Nilsson, D., Uhlen, F., Vogt, U., Hertz, H.M., Schroer, C.G.: Full spatial characterization of a nanofocused X-ray free-electron laser beam by ptychographic imaging. Sci. Rep. **3**, 1633 (2013)
55. Sandberg, R.L., Raymondson, D.A., La, O.V.C., Paul, A., Raines, K.S., Miao, J., Murnane, M.M., Kapteyn, H.C., Schlotter, W.F.: Tabletop soft-X-ray Fourier transform holography with 50 nm resolution. Opt. Lett. **34**(11), 1618–1620 (2009)
56. Williams, G.J., Quiney, H.M., Dahl, B.B., Tran, C.Q., Peele, A.G., Nugent, K.A., De Jonge, M.D., Paterson, D.: Curved beam coherent diffractive imaging. Thin Solid Films **515**(14), 5553–5556 (2007)
57. Williams, G.J., Quiney, H.M., Peele, A.G., Nugent, K.A.: Fresnel coherent diffractive imaging: treatment and analysis of data. New J. Phys. **12**, 035020 (2010)
58. Geilhufe, J., Pfau, B., Schneider, M., Buttner, F., Gunther, C.M., Werner, S., Schaffert, S., Guehrs, E., Frommel, S., Klaui, M., Eisebitt, S.: Monolithic focused reference beam X-ray holography. Nat. Commun. **5**, 3008 (2014)
59. Schlotter, W.F., Rick, R., Chen, K., Scherz, A., Stohr, J., Luning, J., Eisebitt, S., Gunther, C., Eberhardt, W., Hellwig, O., McNulty, I.: Multiple reference Fourier transform holography with soft X-rays. Appl. Phys. Lett. **89**(16), 163112 (2006)
60. Gunther, C.M., Pfau, B., Mitzner, R., Siemer, B., Roling, S., Zacharias, H., Kutz, O., Rudolph, I., Schondelmaier, D., Treusch, R., Eisebitt, S.: Sequential femtosecond X-ray imaging. Nat. Photonics **5**(2), 99–102 (2011)
61. Guizar-Sicairos, M., Fienup, J.R.: Holography with extended reference by autocorrelation linear differential operation. Opt. Express **15**(26), 17592–17612 (2007)
62. Gauthier, D., Guizar-Sicairos, M., Ge, X., Boutu, W., Carre, B., Fienup, J.R., Merdji, H.: Single-shot Femtosecond X-ray holography using extended references. Phys. Rev. Lett. **105**(9), 093901 (2010)
63. Zhu, D., Guizar-Sicairos, M., Wu, B., Scherz, A., Acremann, Y., Tyliszczak, T., Fischer, P., Friedenberger, N., Ollefs, K., Farle, M., Fienup, J.R., Stohr, J.: High-resolution X-ray lensless imaging by differential holographic encoding. Phys. Rev. Lett. **105**(4), 043901 (2010)
64. Wachulak, P.W., Marconi, M.C., Bartels, R.A., Menoni, C.S., Rocca, J.J.: Holographic imaging with a nanometer resolution using compact table-top EUV laser. Opto-Electron. Rev. **18**(1), 80–90 (2010)

65. Schnars, U., Jueptner, W.: Digital Holography: Digital Hologram Recording, Numerical Reconstruction, and Related Techniques. Springer, Berlin (2005)
66. Morlens, A.S., Gautier, J., Rey, G., Zeitoun, P., Caumes, J.P., Kos-Rosset, M., Merdji, H., Kazamias, S., Casson, K., Fajardo, M.: Submicrometer digital in-line holographic microscopy at 32 nm with high-order harmonics. Opt. Lett. **31**(21), 3095–3097 (2006)
67. Genoud, G., Guilbaud, O., Mengotti, E., Pettersson, S.G., Georgiadou, E., Pourtal, E., Wahlstroem, C.G., L'Huillier, A.: XUV digital in-line holography using high-order harmonics. Appl. Phys. B **90**(3–4), 533–538 (2008)
68. Schnars, U., Juptner, W.P.: Digital recording and reconstruction of holograms in hologram interferometry and shearography. Appl. Opt. **33**(20), 4373–4377 (1994)
69. Schnars, U., Jueptner, W.: Direct recording of holograms by a CCD target and numerical reconstruction. Appl. Opt. **33**(2), 179–181 (1994)
70. Garcia-Sucerquia, J., Xu, W., Jericho, S.K., Klages, P., Jericho, M.H., Kreuzer, H.J.: Digital in-line holographic microscopy. Appl. Opt. **45**(5), 836–850 (2006)
71. Schuermann, M.: Digital in-line holographic microscopy with various wavelengths and point sources applied to static and fluidic specimens. Ph.D. thesis, University of Heidelberg (2007)
72. Poon, T.C., Banerjee, P.P.: Contemporary Optical Image Processing with MATLAB. Elsevier Science, Oxford (2001)
73. Liu, G., Scott, P.D.: Phase retrieval and twin-image elimination for in-line Fresnel holograms. J. Opt. Soc. Am. A **4**(1), 159–165 (1987)
74. Koren, G., Polack, F., Joyeux, D.: Iterative algorithms for twin-image elimination in in-line holography using finite-support constraints. J. Opt. Soc. Am. A **10**(3), 423–433 (1993)
75. Rong, L., Li, Y., Liu, S., Xiao, W., Pan, F., Wang, D.Y.: Iterative solution to twin image problem in in-line digital holography. Opt. Laser. Eng. **51**(5), 553–559 (2013)
76. Kreuzer, H.J., Jericho, M.J., Meinertzhagen, I.A., Xu, W.B.: Digital in-line holography with photons and electrons. J. Phys. Condens. Matter **13**(47), 10729–10741 (2001)
77. Kanka, M.: Bildrekonstruktion in der digitalen inline-holografischen Mikroskopie. Universitaetsverlag Ilmenau, Ilmenau (2011)
78. Thibault, P., Dierolf, M., Menzel, A., Bunk, O., David, C., Pfeiffer, F.: High-resolution scanning X-ray diffraction microscopy. Science **321**(5887), 379–382 (2008)
79. Thibault, P., Menzel, A.: Reconstructing state mixtures from diffraction measurements. Nature **494**(7435), 68–71 (2013)
80. Abbey, B., Nugent, K.A., Williams, G.J., Clark, J.N., Peele, A.G., Pfeifer, M.A., De Jonge, M., McNulty, I.: Keyhole coherent diffractive imaging. Nat. Phys. **4**(5), 394–398 (2008)
81. Seaberg, M.D., Zhang, F., Gardner, D.F., Shannon, C.E., Murnane, M.M., Kapteyn, H.C., Adams, D.E.: Tabletop nanometer extreme ultraviolet imaging in an extended reflection mode using coherent fresnel ptychography, pp. 1–9. arXiv: 1312.2049 (2013)
82. Zhang, B., Seaberg, M.D., Adams, D.E., Gardner, D.F., Shanblatt, E.R., Shaw, J.M., Chao, W., Gullikson, E.M., Salmassi, F., Kapteyn, H.C., Murnane, M.M.: Full field tabletop EUV coherent diffractive imaging in a transmission geometry. Opt. Express **21**(19), 21970–21980 (2013)
83. Miao, J.W., Charalambous, P., Kirz, J., Sayre, D.: Extending the methodology of X-ray crystallography to allow imaging of micrometre-sized non-crystalline specimens. Nature **400**(6742), 342–344 (1999)
84. Shapiro, D., Thibault, P., Beetz, T., Elser, V., Howells, M., Jacobsen, C., Kirz, J., Lima, E., Miao, H., Neiman, A.M., Sayre, D.: Biological imaging by soft X-ray diffraction microscopy. Proc. Natl. Acad. Sci. USA **102**(43), 15343–15346 (2005)
85. Huang, X., Nelson, J., Kirz, J., Lima, E., Marchesini, S., Miao, H., Neiman, A.M., Shapiro, D., Steinbrener, J., Stewart, A., Turner, J.J., Jacobsen, C.: Soft X-ray diffraction microscopy of a frozen hydrated yeast cell. Phys. Rev. Lett. **103**(19), 198101 (2009)
86. Raines, K.S., Salha, S., Sandberg, R.L., Jiang, H., Rodriguez, J.A., Fahimian, B.P., Kapteyn, H.C., Du, J., Miao, J.: Three-dimensional structure determination from a single view. Nature **463**(7278), 214–217 (2010)

87. Jiang, H., Song, C., Chen, C.C., Xu, R., Raines, K.S., Fahimian, B.P., Lu, C.H., Lee, T.K., Nakashima, A., Urano, J., Ishikawa, T., Tamanoi, F., Miao, J.: Quantitative 3D imaging of whole, unstained cells by using X-ray diffraction microscopy. Proc. Natl. Acad. Sci. USA **107**(25), 11234–11239 (2010)
88. Chapman, H.N., Barty, A., Bogan, M.J., Boutet, S., Frank, M., Hau-Riege, S.P., Marchesini, S., Woods, B.W., Bajt, S., Benner, H., London, R.A., Plonjes, E., Kuhlmann, M., Treusch, R., Dusterer, S., Tschentscher, T., Schneider, J.R., Spiller, E., Moller, T., Bostedt, C., Hoener, M., Shapiro, D.A., Hodgson, K.O., Van der Spoel, D., Burmeister, F., Bergh, M., Caleman, C., Huldt, G., Seibert, M.M., Maia, F.R.N.C., Lee, R.W., Szoke, A., Timneanu, N., Hajdu, J.: Femtosecond diffractive imaging with a soft-X-ray free-electron laser. Nat. Phys. **2**(12), 839–843 (2006)
89. Axford, D., Owen, R.L., Aishima, J., Foadi, J., Morgan, A.W., Robinson, J.I., Nettleship, J.E., Owens, R.J., Moraes, I., Fry, E.E., Grimes, J.M., Harlos, K., Kotecha, A., Ren, J., Sutton, G., Walter, T.S., Stuart, D.I., Evans, G.: In situ macromolecular crystallography using microbeams. Acta Crystallogr. D Biol. Crystallogr. **68**(5), 592–600 (2012)
90. Ziaja, B., Chapman, H.N., Faeustlin, R., Hau-Riege, S., Jurek, Z., Martin, A.V., Toleikis, S., Wang, F., Weckert, E., Santra, R.: Limitations of coherent diffractive imaging of single objects due to their damage by intense X-ray radiation. New J. Phys. **14**, 115015 (2012)
91. Neutze, R., Wouts, R., van der Spoel, D., Weckert, E., Hajdu, J.: Potential for biomolecular imaging with femtosecond X-ray pulses. Nature **406**(6797), 752–757 (2000)
92. Miao, J., Hodgson, K.O., Sayre, D.: An approach to three-dimensional structures of biomolecules by using single-molecule diffraction images. Proc. Natl. Acad. Sci. USA **98**(12), 6641–6645 (2001)
93. Boutet, S., Lomb, L., Williams, G.J., Barends, T.R.M., Aquila, A., Doak, R.B., Weierstall, U., DePonte, D.P., Steinbrener, J., Shoeman, R.L., Messerschmidt, M., Barty, A., White, T.A., Kassemeyer, S., Kirian, R.A., Seibert, M.M., Montanez, P.A., Kenney, C., Herbst, R., Hart, P., Pines, J., Haller, G., Gruner, S.M., Philipp, H.T., Tate, M.W., Hromalik, M., Koerner, L.J., van Bakel, N., Morse, J., Ghonsalves, W., Arnlund, D., Bogan, M.J., Caleman, C., Fromme, R., Hampton, C.Y., Hunter, M.S., Johansson, L.C., Katona, G., Kupitz, C., Liang, M.N., Martin, A.V., Nass, K., Redecke, L., Stellato, F., Timneanu, N., Wang, D.J., Zatsepin, N.A., Schafer, D., Defever, J., Neutze, R., Fromme, P., Spence, J.C.H., Chapman, H.N., Schlichting, I.: High-resolution protein structure determination by serial femtosecond crystallography. Science **337**(6092), 362–364 (2012)
94. Barends, T.R., Foucar, L., Botha, S., Doak, R.B., Shoeman, R.L., Nass, K., Koglin, J.E., Williams, G.J., Boutet, S., Messerschmidt, M., Schlichting, I.: De novo protein crystal structure determination from X-ray free-electron laser data. Nature **505**(7482), 244–247 (2014)
95. Sandberg, R.L., Paul, A., Raymondson, D.A., Haedrich, S., Gaudiosi, D.M., Holtsnider, J., Tobey, R.I., Cohen, O., Murnane, M.M., Kapteyn, H.C., Song, C.G., Miao, J.W., Liu, Y.W., Salmassi, F.: Lensless diffractive imaging using tabletop coherent high-harmonic soft-X-ray beams. Phys. Rev. Lett. **99**(9), 098103 (2007)
96. Abbey, B., Whitehead, L.W., Quiney, H.M., Vine, D.J., Cadenazzi, G.A., Henderson, C.A., Nugent, K.A., Balaur, E., Putkunz, C.T., Peele, A.G., Williams, G.J., McNulty, I.: Lensless imaging using broadband X-ray sources. Nat. Photonics **5**(7), 420–424 (2011)
97. Chen, B., Dilanian, R.A., Teichmann, S., Abbey, B., Peele, A.G., Williams, G.J., Hannaford, P., Van Dao, L., Quiney, H.M., Nugent, K.A.: Multiple wavelength diffractive imaging. Phys. Rev. A **79**(2), 023809 (2009)
98. Ravasio, A., Gauthier, D., Maia, F.R., Billon, M., Caumes, J.P., Garzella, D., Geleoc, M., Gobert, O., Hergott, J.F., Pena, A.M., Perez, H., Carre, B., Bourhis, E., Gierak, J., Madouri, A., Mailly, D., Schiedt, B., Fajardo, M., Gautier, J., Zeitoun, P., Bucksbaum, P.H., Hajdu, J., Merdji, H.: Single-shot diffractive imaging with a table-top femtosecond soft X-ray laser-harmonics source. Phys. Rev. Lett. **103**(2), 028104 (2009)
99. Malm, E.B., Monserud, N.C., Brown, C.G., Wachulak, P.W., Xu, H., Balakrishnan, G., Chao, W., Anderson, E., Marconi, M.C.: Tabletop single-shot extreme ultraviolet Fourier transform holography of an extended object. Opt. Express **21**(8), 9959–9966 (2013)

100. Seaberg, M.D., Adams, D.E., Townsend, E.L., Raymondson, D.A., Schlotter, W.F., Liu, Y.W., Menoni, C.S., Rong, L., Chen, C.C., Miao, J.W., Kapteyn, H.C., Murnane, M.M.: Ultrahigh 22 nm resolution coherent diffractive imaging using a desktop 13 nm high harmonic source. Opt. Express **19**(23), 22470–22479 (2011)
101. Tobey, R.I., Siemens, M.E., Cohen, O., Murnane, M.M., Kapteyn, H.C., Nelson, K.A.: Ultrafast extreme ultraviolet holography: dynamic monitoring of surface deformation. Opt. Lett. **32**(3), 286–288 (2007)
102. Prell, J.S., Borja, L.J., Neumark, D.M., Leone, S.R.: Simulation of attosecond-resolved imaging of the plasmon electric field in metallic nanoparticles. Ann. Phys. (Berlin) **525**(1–2), 151–161 (2013)

http://www.springer.com/978-3-319-12387-5

High-Resolution Extreme Ultraviolet Microscopy
Imaging of Artificial and Biological Specimens with
Laser-Driven Ultrafast XUV Sources
Zürch, M.W.
2015, XVIII, 127 p. 44 illus., 30 illus. in color., Hardcover
ISBN: 978-3-319-12387-5